Physics-Informed Multimodal Framework for Estimating Human Arm Endpoint Impedance During Physical Human-Robot Interaction

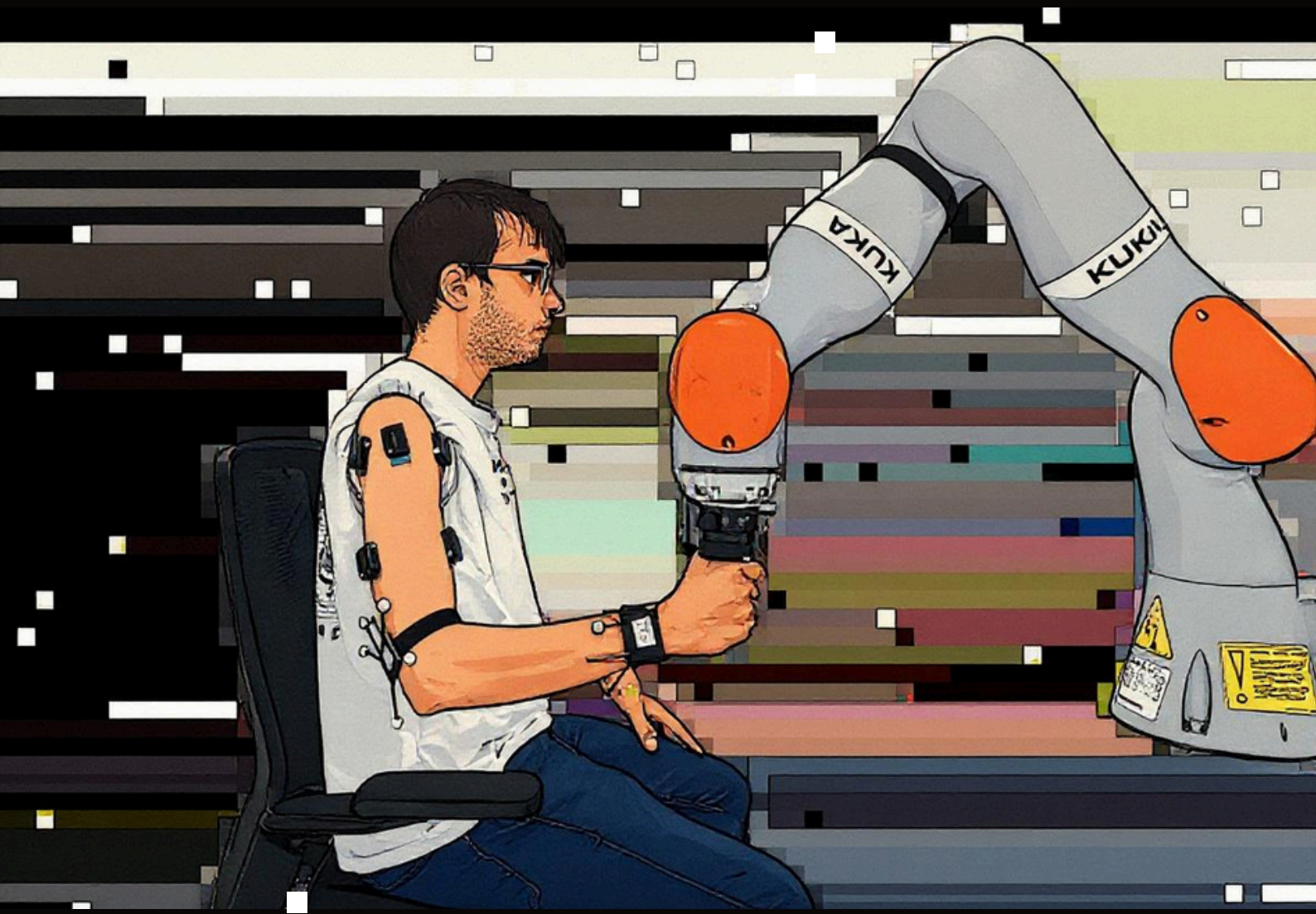

Master Thesis

Aditya Srivastava

TU Delft Delft University of Technology

Physics-Informed Multimodal Framework for Estimating Human Arm Endpoint Impedance During Physical Human-Robot Interaction

Master Thesis

by

Aditya Srivastava

To obtain the degree of Master of Science at the Delft University of Technology, to be defended on 31st October, 2025, at 15:00.

Student Number:	5960932
Main Supervisor/Chair Committee:	Dr. J. Micah Prendergast
Mentor/Committee:	Yuxuan Hu
External Committee:	Dr. Ajay Seth
Faculty:	Mechanical Engineering

TU Delft Delft University of Technology

Preface

“I may not have gone where I intended to go, but I think I have ended up where I needed to be.”

— Douglas Adams

It would be too short a space to describe everything I have experienced in the past two years. Coming to the Netherlands for my master’s has been one of the best decisions of my life. This place has given me so much; it challenged me, pushed me out of my comfort zone, and helped me grow both academically and personally.

This thesis marks the end of my Master’s journey at TU Delft, made possible with the support of so many people, to whom I’m truly grateful. I started with just a vague idea of doing something with human-robot interaction and biomechanics, and I’m thankful to my supervisor, Dr. J. Micah Prendergast, for giving me the freedom to explore, for listening to my ideas, and for believing in me throughout. It’s because of your patience and guidance that this work became what it is now.

A big thanks to Yuxuan, who constantly came to the lab to check if I needed help. Thank you for guiding me through iterations and helping me set up the experiment. My thanks also go to my colleagues and the members of Lab 34.F-0-460. To my friends here in Delft and back home, this journey wouldn’t have been the same without you.

Grandparents, thank you for your love and blessing. To my parents, a simple “thank you” will never be enough for all the sacrifices you’ve made but thank you for always believing in me. To my sister, my biggest cheerleader and best friend, this couldn’t have been done without you. And finally, to our cat Miu-Miu, thank you for simply existing.

Aditya Srivastava

Delft, October 2025

Author’s Note: Parts of the text were refined with the assistance of ChatGPT 5 (OpenAI) to improve clarity and readability. All ideas, analyses, and conclusions are entirely the author’s own. AI tools were not used for data collection or analysis, and the author takes full responsibility for the final content.

Content

Report

Physics-Informed Multimodal Framework for Estimating Human Arm Endpoint Impedance During Physical Human-Robot Interaction

Aditya Srivastava

***Abstract*—Humans can adapt their hand compliance dynamically according to task demands by modulating arm endpoint impedance through changes in arm configuration and muscle co-contraction. This work introduces a multimodal physics-informed machine learning framework for estimating human arm endpoint impedance during multi-degree-of-freedom interaction with a collaborative robot. In this pilot study, data were collected during static and dynamic interaction tasks with the robot. During each trial, muscle activity was recorded via surface electromyography (sEMG), joint kinematics were measured via motion capture (MoCap), interaction forces were recorded with a force sensor, and end-effector positions were obtained directly from the robot. The neural network models were trained to predict the impedance parameters identified from a perturbation-based experiment using these multimodal inputs. Two models were developed and compared: a Temporal Convolutional Network with Multi-Layer Perceptron head (TCN-MLP) as a baseline and a Temporal Convolutional Network Physics-Informed Neural Network (TCN-PINN) that integrates physical consistency through a physics-based loss term.**

Results show that introducing the physics constraint improved the prediction accuracy of the inertia (M), damping (D), and stiffness (K) parameters compared to the purely data-driven model. The inclusion of dynamic movement trials preserved model stability and generalization. While the estimated parameters are not yet accurate enough for direct implementation, the limitations are analyzed and used to identify directions for achieving more consistent and robust results. Nonetheless, the findings indicate that the proposed physics-informed multimodal learning framework has strong potential for estimating human arm endpoint impedance during multi-joint, dynamic physical human-robot interaction.

***Index Terms*—Physical human-robot interaction, arm endpoint impedance, physics-informed neural network**

I Introduction

Estimating human arm endpoint impedance has been a key research goal in biomechanics and human-robot interaction for the past three decades [1]–[5]. The endpoint impedance describes the dynamic relationship between small perturbations in hand position and the resulting interaction forces, commonly parameterized to inertia (M, kg), damping (D, N·s/m), and stiffness (K, N/m). Humans possess the ability to modulate these parameters, collectively referred to as compliance, according to the demands of a task [6]–[8]. The central nervous system (CNS) regulates the limb dynamics by changing the arm configuration and modulating muscle activation/co-contraction to maintain stability and precision under varying environmental conditions [4], [9].

The author is with Delft University of Technology, a.srivastava-16@student.tudelft.nl

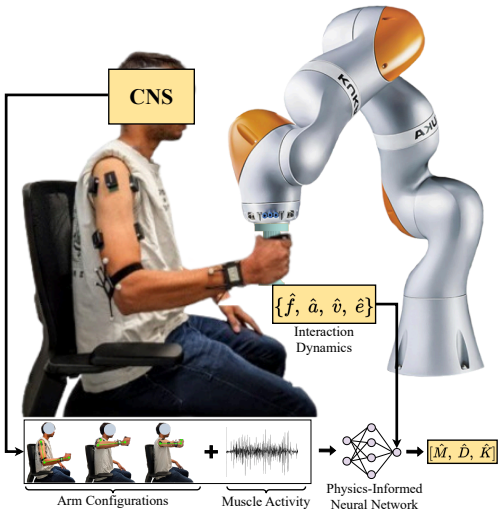

Fig. 1. During the physical human-robot interaction, the central nervous system regulates muscle activation and arm configuration, which together determine the arm's dynamic properties, i.e., inertia (M), damping (D), and stiffness (K). These measurable modalities (muscle activity and arm joint kinematics) can serve as inputs to a physics-informed neural network, which incorporates force and kinematic data within its loss function to ensure physically consistent estimation of the arm's endpoint impedance parameters.

With the increasing use of collaborative robots (cobots) in shared workspaces, especially for tasks that cannot be fully automated, understanding and replicating human adaptability has become critical [10]. Physical human-robot interaction (pHRI) applications, such as rehabilitation and assistive robotics, require robots to respond safely and intuitively to human motion and interaction forces [11], [12]. As a result, incorporating human endpoint impedance into pHRI control enables robots to interact with humans naturally and adapt to their mechanical behavior [13]–[15].

In physical human-robot interaction (pHRI), multiple joints contribute to the endpoint behavior, and their coupled dynamics determine the overall impedance of the hand [16]. The most established approach for estimating multi-joint human arm impedance is the perturbation paradigm, in which controlled force or position perturbations are applied to the hand while recording the resulting motion response. The endpoint impedance is then identified by fitting the relationship between force and kinematic deviations to a second-order mass-damper-spring model, yielding the inertial (M), damping (D), and stiffness (K) parameters [1], [2], [17], [18].

In static postural tasks, where the limb maintains a fixed configuration, impedance estimation typically focuses on stiffness. During the quasi-steady plateau phase of the perturbation, when velocity and acceleration components are negligi-

ble, the stiffness can be approximated by the linear relation between force and displacement [19]. For full impedance estimation, more sophisticated perturbation protocols model the arm as a multi-joint mechanical system and identify the dynamic parameters by regression or frequency-domain fitting. Examples include the use of polynomial approximations [5], [20] and stochastic perturbations [21].

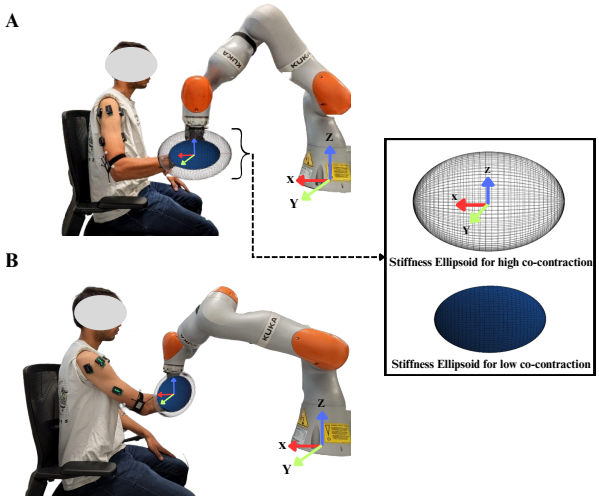

Fig. 2. The size of the ellipsoid represents the magnitude of the endpoint stiffness; the blue ellipsoid represents the low co-contraction among the antagonistic pair, and the gray one represents when there is high co-contraction. In the image at the top, the principal direction of the stiffness is along the x-axis, whereas at the bottom, the principal direction is along the y-axis. This shows that it changes with the arm configuration.

When the interaction task is dynamic, estimating impedance becomes difficult because it continuously varies with motion and muscle activation. Accurate identification requires precise knowledge of the unperturbed trajectory [2], [7]. Both position-based and force-based perturbations have been employed to estimate time-varying impedance in such conditions [7], [9]. Although these perturbation-based methods remain the standard for biomechanical accuracy, they are impractical for natural or continuous multi-joint movements.

An alternative approach for estimating human arm impedance is to map muscle activity, measured via electromyography (EMG), to the mechanical parameters of the limb [22]–[24]. Because EMG reflects neural drive to muscles, it provides an indirect indication of muscle tension and activation, both of which influence endpoint stiffness [25]. In this approach, processed EMG features, typically corrected and normalized activations of pairs of antagonistic muscles, are related to impedance parameters through biomechanical muscle models or data-driven regression frameworks [8], [23], [26]–[28].

The key advantage of EMG-based estimation is that it can be performed during unperturbed, continuous motion, since impedance modulation arises from voluntary muscle activation rather than external perturbations. Mapping of human arm stiffness to the stiffness parameters of a remote robot manipulator by EMG in real time was introduced in the tele-impedance application [26]; although not a direct contact-based pHRI scenario [29], it demonstrated the capability of transferring the human impedance parameter using EMG. Later, a reduced-complexity five-degree-of-freedom (5-DOF) model was proposed to estimate human endpoint stiffness by combining joint angles with normalized EMG signals, enabling real-time stiffness adaptation during multi-joint interactions [27]. More recently, a simplified model estimated endpoint stiffness in three Cartesian directions from forearm co-contraction levels and arm configuration and validated through perturbation-based identification experiments [8].

However, most EMG-based mappings focus primarily on stiffness estimation, as damping and inertial components cannot be inferred directly from muscle activation alone. Moreover, these models typically require subject-specific calibration and are trained or identified offline using perturbation-based datasets before being deployed for real-time inference [8], [26], [27]. While such methods estimate impedance without interrupting movement, their reliance on empirically derived mappings and offline tuning limits their ability to generalize to complex, dynamic interaction scenarios.

Data-driven machine learning models can similarly learn the mapping between multimodal signals and impedance parameters when trained offline and subsequently deployed for real-time estimation. As discussed earlier, numerous studies have demonstrated that arm endpoint impedance is influenced by arm configuration and muscle co-contraction level. Endpoint stiffness, in particular, is strongly affected by these factors, which jointly determine both the magnitude and directional anisotropy of stiffness, typically represented as an ellipsoid in Cartesian space, as shown in Fig. 2. Utilizing the relationships between muscle activity and joint kinematics, therefore, could provide a pragmatic estimate of human impedance in dynamic, multi-joint contexts.

Previous work has explored this concept using machine learning approaches. For instance, mapping EMG and joint angles of participants interacting with an exoskeleton helped the estimation of joint stiffness during multi-joint movements without applying perturbations [30]; however, the study was limited to a two-degree-of-freedom (2-DOF) setup in which the arm motion was constrained by an exoskeleton, which is not ideal for pHRI scenarios. More recently, a study combined sEMG features with elbow joint angle to estimate endpoint stiffness, demonstrating the feasibility of EMG-kinematic fusion for impedance prediction in single-joint, unconstrained motion [31]. However, the estimated stiffness in that work was derived from model-generated rather than experimentally measured ground truth, limiting its physical interpretability.

Although data-driven models can represent complex nonlinear relationships, they often function as black-box systems without explicit modeling of the underlying neuromechanical mechanisms [32]. Integrating a human model in the pHRI can lead the robot to improved human understanding and better functionalities [12]. Thus, utilizing physics-informed machine learning methods could offer the best of both worlds: a data-driven model constrained by physical laws, allowing generalization to more uncertain conditions while maintaining physically plausible boundaries [33], [34]. Recent studies have successfully applied physics-informed neural networks

(PINNs) in the biomechanical domain to predict joint kinematics and muscle forces [32], [35], demonstrating their potential to infer underlying biomechanical parameters in a physically consistent manner.

Previous data-driven studies have primarily addressed either single-joint motion or constrained multi-joint movement for impedance estimation. In this study, we developed a multimodal learning framework for estimating human arm endpoint impedance during unconstrained, multi-joint physical human-robot interaction. The framework integrates surface electromyography (sEMG), joint kinematics, and interaction forces measured from a collaborative robot to estimate the dynamic impedance parameters, inertial (M), damping (D), and stiffness (K) for both static and dynamic interactions while establishing a concrete ground truth. We designed a physics-informed neural network (PINN) that embeds the governing mass-damper-spring relationship directly into the learning objective, ensuring that model predictions remain plausibly physically consistent. The framework proposes a Temporal Convolutional Network Physics-Informed Neural Network (TCN-PINN) architecture, which combines temporal feature extraction from multimodal signals with physics-based constraints to capture the time-dependent behavior of human impedance. In parallel, for comparison, we also implement a Temporal Convolutional Network Multi-Layer Perceptron (TCN-MLP), a purely data-driven model as a baseline without physics integration. The goal of this study is to investigate whether incorporating physical priors into a data-driven network can improve human arm endpoint impedance estimation compared to conventional black-box approaches.

II Methodology

This section gives a complete overview of the proposed framework, divided into two subsections. Section II-A describes the methodology for estimating human arm endpoint impedance, including the experiment setup, protocol, and identification technique that are used to establish the ground truth. Section II-B presents the architecture of the proposed neural network models, i.e., TCN-MLP and TCN-PINN, and the evaluation criteria to assess their performance. The complete framework is illustrated in Fig. 3.

II-A Arm Endpoint Estimation during pHRI

The first step toward multimodal estimation of impedance is obtaining the reference (ground-truth) endpoint impedance values, used to train the models. In this study, endpoint impedance was estimated independently along each Cartesian axis ($\pm x$, $\pm y$, $\pm z$). This estimation approach follows established perturbation-based impedance identification methods in physical human-robot interaction [7], [36]. Estimating impedance per axis decouples the identification problem, enabling stable least-squares estimation of the inertial (M), damping (D), and stiffness (K) parameters within short analysis windows. Modeling all six cross-axis coupling terms would require perturbations in multiple directions and longer recordings, which often introduce voluntary motion responses and reduce estimation reliability [36]. The single-axis approach, therefore, provides physically meaningful, direction-specific impedance parameters while maintaining experimental tractability and consistency with prior literature.

II-A.1 Experimental Setup

The complete experimental setup is shown in Fig. 4. It consisted of a KUKA LBR iiwa 7 R800 collaborative robot (KUKA AG, Augsburg, Germany), a Bota Systems SenseOne six-axis force/torque (F/T) sensor (Bota Systems AG, Zurich, Switzerland) mounted at the robot end-effector, an OptiTrack Prime 13W motion capture system (NaturalPoint Inc., Corvallis, OR, USA), and Trigno Avanti wireless surface EMG sensors (Delsys Inc., Natick, MA, USA).

The KUKA LBR iiwa 7 was controlled in Cartesian space using an impedance controller implemented through the Robot Operating System (ROS) and the Fast Research Interface (FRI) at 200 Hz. In perturbation-based impedance estimation, either position-controlled [20], [37] or admittance-controlled [7], [36] schemes are commonly employed. In this study, a Cartesian impedance controller was selected, as it provides a stable and well-defined dynamic behavior of the robot while

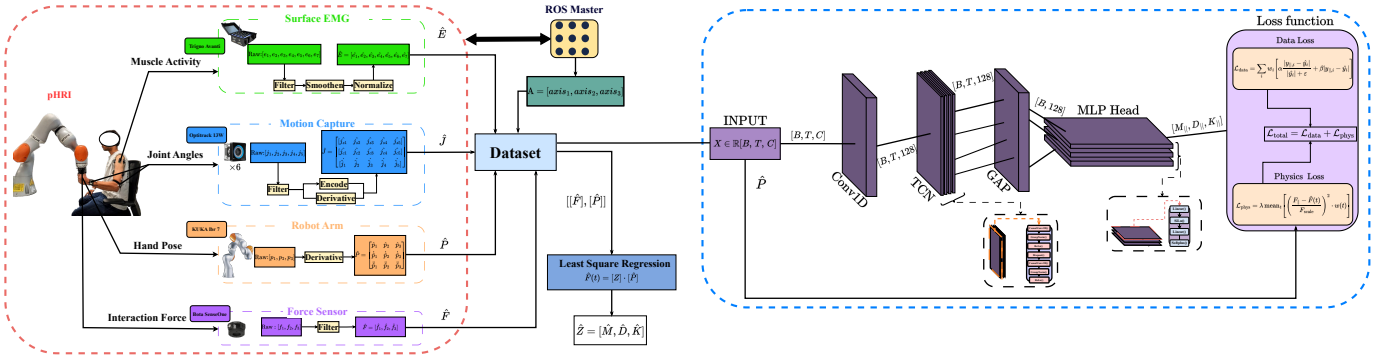

Fig. 3. Proposed multimodal framework for human arm endpoint impedance estimation. **Left:** Experimental setup and data collection for physical human-robot interaction using EMG, motion capture, and force sensing. **Right:** Architecture of the proposed TCN-PINN model trained on the processed dataset alongside least-squares identification results.

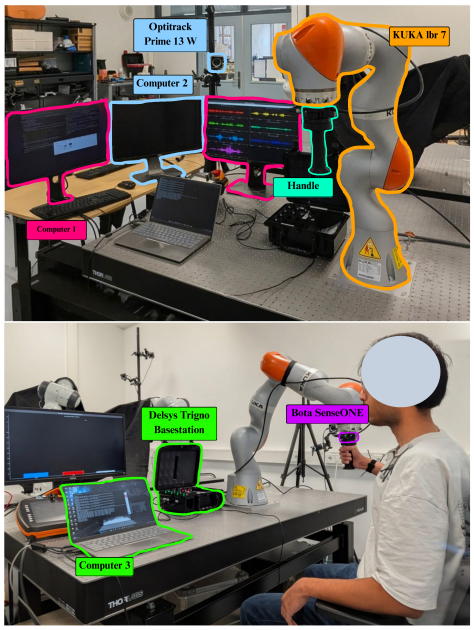

Fig. 4. The image shows the complete setup used in the experiment. During the interaction with the robot, the subject modulates muscle co-contraction according to the task requirements while receiving visual feedback on a display.

allowing compliant interaction with the human. By regulating the robot to behave as a virtual mass-spring-damper system, the controller ensures safety and transparency during contact while injecting perturbation forces. Unlike pure position control, it allows measurable end-effector displacements in response to human impedance, and unlike admittance control, it does not rely on high-bandwidth force control. This makes impedance control suitable for estimating human endpoint impedance during physical human-robot interaction using the KUKA LBR platform [38].

The commanded joint torques were computed as,

$$\tau = J^{\mathsf{T}}\big(-Ke - D\dot{x}\big), \tag{1}$$

where J is the end-effector Jacobian, $e = x - x_d$ is the Cartesian pose error, $\dot{x}$ is the end-effector velocity, and K and D are the stiffness and damping matrices, respectively. This control law makes the robot behave as a virtual mass-spring-damper system in task space, allowing the end-effector to deviate compliantly when external forces are applied. A secondary (null-space) control was implemented to maintain the desired joint posture and compensate for gravity without interfering with the end-effector motion. Together, these components ensure stable and transparent interaction behavior suitable for estimating human endpoint impedance during physical human-robot interaction.

For this experiment, only the five degrees of freedom of the human arm were captured, as wrist muscles contribute minimally to endpoint stiffness compared to the shoulder and elbow muscles [28]. The computed joint motions included shoulder flexion/extension, abduction/adduction, internal/external rotation, elbow flexion/extension, and forearm pronation/supination. To record joint kinematics, six OptiTrack Prime 13W cameras were positioned around the workspace to track cluster markers placed on the shoulder, upper arm, and forearm, at a sampling rate of 240 Hz (Fig. 5).

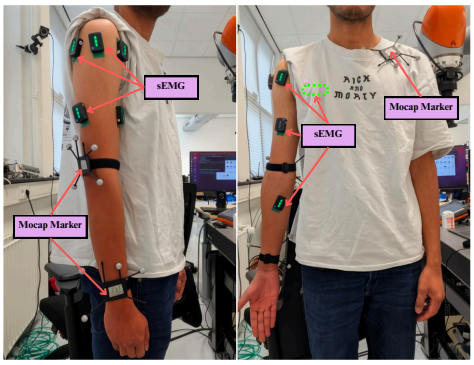

Fig. 5. sEMG sensors are positioned according to the SENIAM recommendations, and three rigid marker clusters are placed on the upper arm and forearm to capture their relative orientation with respect to the shoulder marker.

Muscle activity was recorded using surface EMG (sEMG) sensors targeting the posterior, medial, and anterior deltoids; pectoralis major; pronator teres; and the biceps-triceps antagonistic pair. These muscles were selected for their primary roles in generating the recorded joint movements. EMG data were collected at 2148 Hz, and electrode placement (Fig. 5) followed the SENIAM recommendations [39].

The hand position corresponded to the handle attached to the robot end-effector, recorded directly by the robot at 200 Hz. The F/T sensor mounted between the end-effector and handle measured interaction forces at 1000 Hz. All EMG, motion capture, force, and robot data were streamed to a single computer via TCP connection, ensuring synchronized multimodal acquisition. System clocks between the systems were synchronized using a local Network Time Protocol (NTP) server, maintaining timestamp alignment with the computer hosting the ROS master within approximately 5 ms.

II-A.2 Experiment Protocol

To evaluate whether the proposed framework can estimate human arm impedance from multimodal inputs, a single participant was recruited for this pilot experiment. The procedure began with collecting the maximum voluntary isometric contraction (MVIC) of each target muscle. After sensor placement, the subject underwent exercises that activated each target muscle separately to capture the maximum contraction. The exercise was repeated three times with a one-minute rest between repetitions to minimize fatigue. Once all MVIC data were collected, the subject entered the motion capture volume to calibrate the neutral joint position by standing upright with both arms relaxed alongside the body, palms facing the body, and feet parallel and shoulder-width apart.

The experiment consisted of both static and dynamic trials. For the static trials, six distinct arm poses were selected to cover the reachable workspace and represent typical interaction configurations that could be encountered during pHRI (Fig. 6). The subject was seated to stabilize the trunk, ensuring that perturbations were isolated to the arm and not transmitted

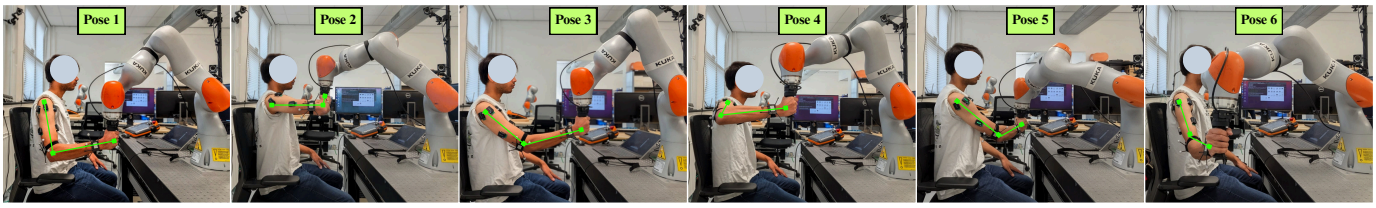

Fig. 6. The static trials are recorded in six distinct arm poses covering the range of the workspace and representing possible interaction configurations encountered during physical human-robot interaction (pHRI).

to the torso. To examine the effect of muscle co-contraction, each static pose was tested under two activation levels: *low* and *high*. During the high-contraction condition, the subject co-contracted the biceps and triceps muscles to increase joint stiffness [40]. Real-time visual feedback of normalized EMG amplitudes was displayed on a monitor to help the subject regulate the co-contraction intensity, as shown in Fig. 4.

Raw EMG from the biceps and triceps, $E_b(t)$ and $E_t(t)$, were full-wave rectified and low-pass smoothed using a 300 ms rolling RMS window to obtain envelopes $\tilde{E}_b(t)$ and $\tilde{E}_t(t)$. Each envelope was then normalized by its maximum voluntary isometric contraction (MVIC), yielding normalized activations,

$$P_b(t) = \frac{\tilde{E}_b(t)}{E_b^{\mathrm{MVIC}}}, \qquad P_t(t) = \frac{\tilde{E}_t(t)}{E_t^{\mathrm{MVIC}}}. \tag{2}$$

The instantaneous co-contraction level was defined by the min-rule [8]:

$$C(t) = \min\big(P_b(t),\, P_t(t)\big), \tag{3}$$

which represents the overlapping portion of antagonist activations. Here, $C(t) = 0$ indicates unilateral activation (a more compliant arm), whereas a larger $C(t)$ indicates stronger activation (greater joint stiffness). Based on pilot distributions, $C < 0.1$ was categorized as low co-contraction and $C \geq 0.1$ as high co-contraction.

Each static pose was repeated ten times under the low co-contraction condition and five times under the high co-contraction condition to minimize fatigue. Each trial lasted 90 s, during which randomized perturbations were applied along the $\pm x$, $\pm y$, and $\pm z$ directions (three per direction) so that the subject could not anticipate the upcoming perturbation.

For the dynamic trials, only the low co-contraction condition was performed, as maintaining high contraction during continuous motion is impractical and does not reflect natural pHRI behavior. In this case, the subject moved the robot handle back and forth along the x-axis following a straight-line trajectory, while perturbations were applied perpendicular to the motion direction. Each dynamic trial was repeated five times, with 18 perturbations per trial.

The Cartesian impedance controller regulated motion through a virtual mass-spring-damper system; thus, the effective perturbation intensity depended on both the robot's intrinsic impedance and that of the human arm, as well as on the perturbation duration. Therefore, the perturbation amplitude and duration were selected to sufficiently excite the arm's dynamics while remaining within the pre-voluntary response window (≤ 115 ms) to exclude voluntary corrections [41] and to keep the peak displacement below 10 mm, preserving the local linearity assumption of the impedance model [2], [41], [42]. Based on these requirements, a commanded force step of 8 N lasting 80 ms was experimentally chosen, with at least 4 s between consecutive perturbations.

For both static and dynamic trials, the robot's translational stiffness (K_t) was set to approximately zero to minimize its influence on the impedance estimation, and the rotational stiffness (K_r) was set to 150 N·m/rad to maintain end-effector orientation and prevent motion coupling across Cartesian axes during perturbation injection. The damping ratio r was set to 0.9. Gravity and inertial compensation were calibrated before the experiment to render the robot effectively weightless to the subject, ensuring that the robot's intrinsic impedance had a negligible effect on the estimation of human arm impedance.

II-A.3 Data Processing and Impedance Identification

After data collection, two main objectives need to be addressed before feeding to the neural network: (*i*) preparing the multimodal dataset to be used as inputs for the neural network, and (*ii*) identifying the data required to compute the impedance parameters that serve as the ground truth.

The raw sEMG signals, recorded at a sampling rate of 2148 Hz, were first band-pass filtered between 20 Hz and 450 Hz to remove motion artifacts and high-frequency noise. The filtered signals were then full-wave rectified to convert all negative oscillations into positive values. Since muscle activation magnitude and co-contraction level directly influence endpoint impedance [9], [26], the rectified EMG signals were smoothed using a root-mean-square (RMS) window of 50 ms to capture the mean power of muscle activity [43]. Finally, each muscle channel was normalized by its respective maximum voluntary isometric contraction (MVIC) value.

Joint kinematics were captured by tracking the rigid-body markers with the motion capture system at 240 Hz. The recorded Cartesian poses were converted to joint-space angles (in radians) through Euler-angle transformations following the anatomical joint definitions. To prevent discontinuities caused by angle wrapping, particularly in shoulder internal/external rotation and forearm pronation/supination, the joint angles were encoded using their sine and cosine representations before being used as neural network inputs. In addition to

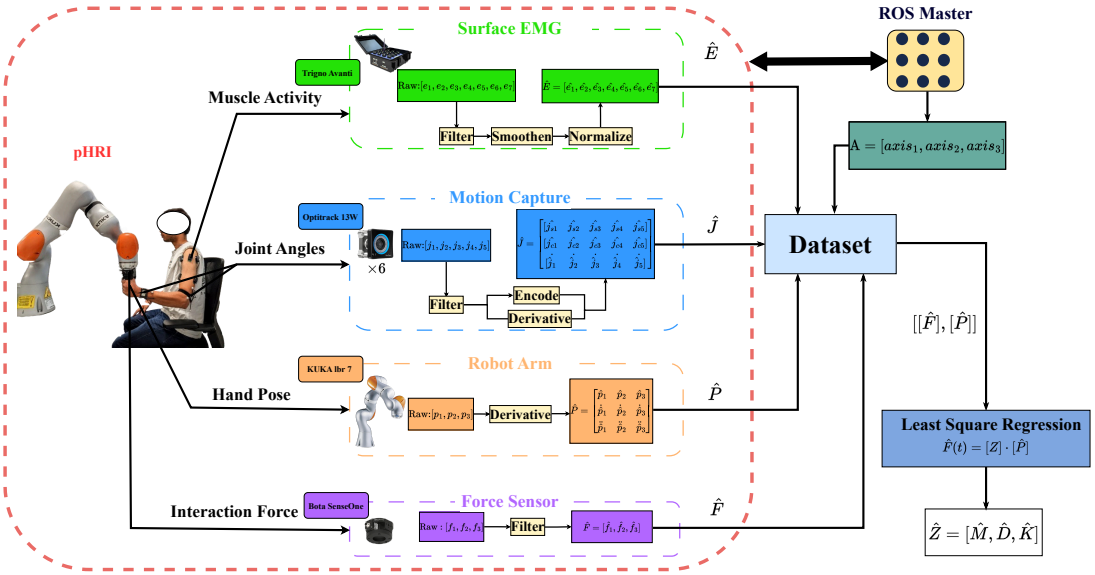

Fig. 7. Complete overview of the physical human-robot interaction experiment. During the perturbation experiment with the robot, muscle activities from seven muscles are recorded using surface electromyography (sEMG), joint kinematics are captured via a marker-based motion capture (MoCap) system, hand pose is obtained from the robot end-effector position, and interaction forces are measured using a six-axis force/torque (F/T) sensor. The perturbation direction and axis information are provided by the ROS master, which also handles all inter-device communication. All recorded modalities are post-processed, synchronized to a common sampling rate of 200 Hz, and stored in a unified dataset. The synchronized position and force data are then used to estimate the ground-truth impedance parameters.

joint positions, joint angular velocities were computed using a third-order Savitzky-Golay derivative filter. Including joint velocities allows the network to account for the dynamic effects of muscle contraction, since muscle force and thus stiffness depend not only on activation and length but also on contraction velocity due to the nonlinear force-velocity relationship [30].

The estimation of the hand pose and interaction force is essential for both ground-truth impedance identification and the physics-informed neural network. The robot end-effector pose $\mathbf{p}(t)$ was recorded at 200 Hz, while velocity and acceleration were derived using a third-order Savitzky-Golay derivative filter to ensure smooth and temporally aligned kinematic signals.

The raw force signals measured by the 6-axis F/T sensor were preprocessed to remove high-frequency noise while preserving human-induced dynamics. The three Cartesian force components (F_x, F_y, F_z) were low-pass filtered using a fourth-order Butterworth filter with an 18 Hz cutoff frequency, determined to retain the bandwidth of human arm dynamics while attenuating sensor noise [44].

After post-processing all raw signals, the data were synchronized and resampled at 200 Hz to align with the robot controller's FRI update rate and to ensure equal vector lengths across modalities before being used as neural network inputs. The corresponding perturbation-axis information (i.e., the direction of the applied force) was appended to each synchronized window to provide the network with contextual information about the perturbation direction, which is crucial for learning axis-dependent impedance behavior.

From the synchronized dataset (force, pose, velocity, acceleration, and axis labels), endpoint impedance was estimated for each perturbation window. Each window was anchored at the detected force onset (t_0), followed by a 15 ms guard period to exclude onset transients. Although each perturbation impulse lasted approximately 80 ms and voluntary human responses typically occur after about 100 ms [45], the number of data samples within that short interval was insufficient for a stable regression, resulting in unrealistic parameter values. Therefore, impedance estimation was performed over extended time frames ranging from 80 ms to 320 ms with 20 ms increments, and the most physically consistent results were obtained using a 260 ms analysis window. This choice also aligns with previous impedance estimation studies employing similar perturbation durations [7].

Pre-window baselines for force, velocity, and acceleration were computed over the 25 ms preceding t_0 and subtracted to obtain baseline-corrected signals. The signed perturbation axis ($\pm x$, $\pm y$, $\pm z$) was inferred from the axis channels and used to project all signals onto the dominant direction, yielding $(\hat{f}, \hat{a}, \hat{v}, \hat{e})$ corresponding to the force, acceleration, velocity, and displacement along the perturbation axis. For each window, impedance parameters were obtained using ordinary least squares:

$$\hat{f}(t) \;\approx\; \hat{M}\,\hat{a}(t) + \hat{D}\,\hat{v}(t) + \hat{K}\,\hat{e}(t), \tag{4}$$

where $\hat{M}$, $\hat{D}$, and $\hat{K}$ represent the estimated inertia, damping, and stiffness, respectively. All non-positive parameter values were discarded and excluded from the neural network training dataset. The valid impedance estimates were stored alongside the synchronized multimodal signals to serve as ground truth for both model training and evaluation.

The complete ground truth estimation experiment setup and data processing pipeline is illustrated in Fig. 7.

II-B Neural Network Model

In the proposed framework, illustrated in Fig. 3, the architecture of Temporal Convolutional Network Physics-Informed Neural Network (TCN-PINN) is presented. The clear layer configurations are shown in Fig. 8 and Fig. 9. In addition, a purely data-driven baseline model, termed the Temporal Convolutional Network Multi-Layer Perceptron (TCN-MLP), was also implemented to evaluate the effect of the physics-informed regularization. This serves as a direct evaluation of how incorporating physical constraints in architecture affects predictive accuracy and model generalization.

II-B.1 Architecture Overview

In this study, the network inputs consist of multimodal time series combining surface electromyography (sEMG) signals and joint kinematic information, which together capture the neuromuscular activation and mechanical state of the limb during interaction. Each data sample represents a short temporal window of synchronized recordings at 200 Hz. After excluding the 15 ms onset guard, each window spans approximately 245 ms, resulting in a sequence of 49 time steps that enclose the transient impedance response.

Given the task demand for capturing the temporal property in short-duration windows, a Temporal Convolutional Network (TCN) architecture was adopted [46]. Unlike static feedforward models that process each frame independently, TCN uses dilated causal convolutions that allow the model to capture time-dependent relationships, such as how changes in muscle activation and joint velocity jointly influence endpoint stiffness while maintaining strict temporal causality. The input tensor $\mathbf{X} \in \mathbb{R}^{B\times T\times C}$, where B is the batch size and $T = 49$, contains C feature channels corresponding to different input modalities. This configuration allows the convolutional filters to capture the temporal evolution of both EMG and kinematic features over roughly a quarter of a second.

Two architectures were developed under a common temporal encoder to evaluate the impact of physical consistency within the learning framework. The first, a purely data-driven model (TCN-MLP), learns the statistical mapping between multimodal input sequences and impedance parameters solely from data. The second, the physics-informed model (TCN-PINN), extends this design by introducing a physics-consistency branch that constrains the predictions to satisfy the governing mass-damper-spring relationship between motion and force. Both models share the same temporal feature extraction strategy based on causal convolutions, ensuring they learn from identical temporal contexts. Their architectures differ slightly: the TCN-MLP uses a lighter encoder with 64 hidden channels, batch normalization, and a single shared regression head, whereas the TCN-PINN employs a deeper encoder with 128 channels, group normalization, and separate regression heads for each impedance component, together with the physics-consistency branch. These differences were introduced intentionally to accommodate the additional inputs and physics-based supervision in the TCN-PINN. Therefore, any performance differences between the two models can be attributed primarily to the addition of the physics-informed regularization rather than to differences in temporal modeling. This setup provides a fair and controlled comparison between a purely data-driven estimator and one guided by the physical dynamics of human impedance.

The baseline TCN-MLP serves as a purely data-driven model for predicting the impedance parameters $[M_{\|}, D_{\|}, K_{\|}]$ directly from multimodal temporal features. Each training window $\mathbf{X} \in \mathbb{R}^{B\times T\times C}$ contained $C = 25$ normalized channels consisting of seven EMG features, five joint cosine and sine encodings each, and five joint angular velocities, along with three axis components (x, y, z). Non-axis inputs were z-scored

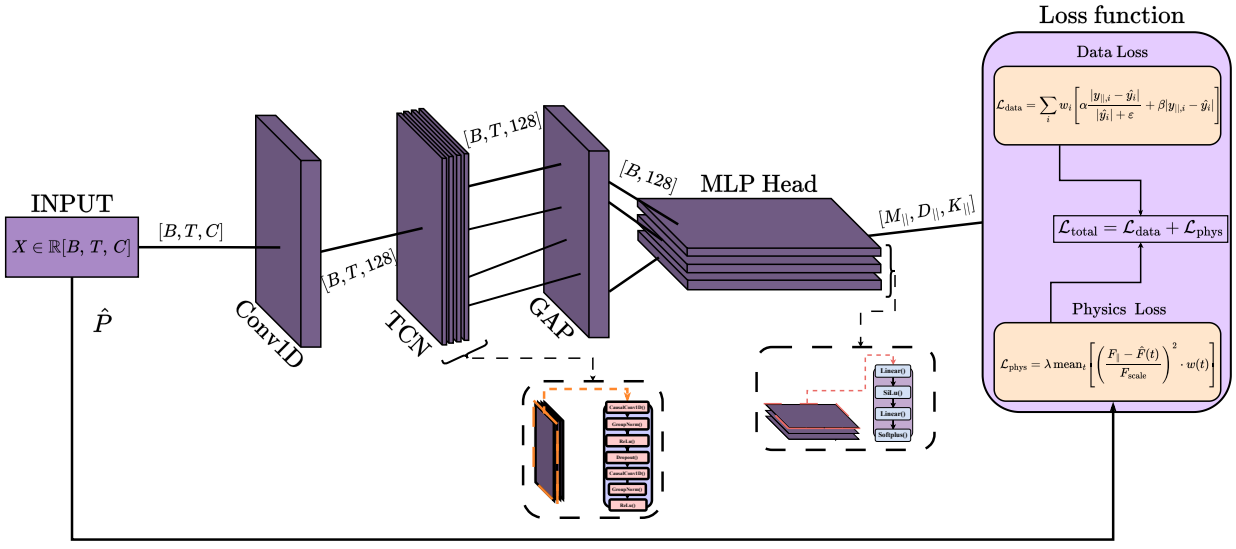

Fig. 8. Architecture of the proposed TCN-PINN. Multimodal inputs are processed by a 1×1 Conv1d layer followed by four causal residual TCN blocks. A global average pooling produces a latent vector that feeds three parallel MLP heads predicting the impedance parameters ($M_{\|}$, $D_{\|}$, $K_{\|}$). The model is trained using a supervised data loss and a physics loss enforcing the mass-damper-spring relation $F_{\|}(t) = M_{\|}\hat{a}(t) + D_{\|}\hat{v}(t) + K_{\|}\hat{e}(t)$.

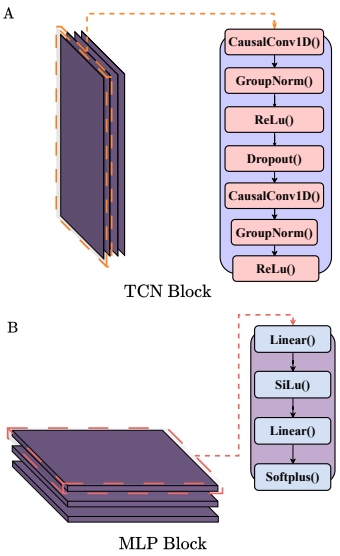

Fig. 9. **(A)** Layer architecture of the TCN block. **(B)** Layer architecture of a single MLP head used to predict M, D, and K.

using training-set statistics, whereas axis features were left unnormalized to preserve their directional meaning.

The model begins with a 1×1 convolutional projection layer that maps the input channels to 64 latent feature maps, followed by a stack of five residual TCN blocks with kernel size 3 and dilations $(1, 2, 4, 8, 16)$. Each block consists of two causal convolutions, each followed by batch normalization, ReLU activation, and dropout ($p = 0.1$), with skip connections maintaining stable gradient propagation. The temporal features extracted by the TCN are aggregated through a global average pooling layer, resulting in a latent vector $\mathbf{h} \in \mathbb{R}^{64}$.

Finally, a multilayer perceptron (MLP) head maps $\mathbf{h}$ to the impedance parameters through $\text{Linear}(64 \to 32) \to \text{ReLU} \to \text{Dropout}(0.1) \to \text{Linear}(32 \to 3)$, producing the predictions $[M_{||}, D_{||}, K_{||}]$. A Softplus activation is applied to ensure non-negative outputs, preserving physical interpretability. This baseline serves as a reference to evaluate how well temporal feature extraction alone can estimate impedance without explicit physics constraints.

Building upon the baseline, the Temporal Convolutional Network Physics-Informed Neural Network (TCN-PINN) extends the architecture by incorporating additional motion and force features, a deeper encoder, and a physics-consistency module that enforces dynamic relationships between motion and interaction forces. Each input sequence $\mathbf{X} \in \mathbb{R}^{B \times T \times C}$, with $T = 49$ and $C = 37$, includes the same EMG and joint features as in the baseline model, supplemented with end-effector pose, velocity, acceleration, and force signals, along with three-axis components. These additional modalities enable the model to learn both the neuromuscular and mechanical contributions to impedance.

The encoder begins with a 1×1 convolutional layer that projects the input to 128 latent channels, followed by four TCN blocks with kernel size 3 and dilations $[1, 2, 4, 8]$. Each block consists of two causal convolutions followed by Group Normalization (GroupNorm(1,128)), ReLU activation, and dropout ($p = 0.1$), the structure of a single TCN block is represented in Fig. 9. The causal padding $(k - 1) \cdot d$ ensures that the receptive field grows only toward the past, maintaining strict temporal causality. The final feature representation is obtained through a global average pooling (GAP) layer, which compresses the temporal features into a latent vector $\mathbf{h} \in \mathbb{R}^{128}$.

From this latent representation, three independent regression heads estimate the impedance parameters through identical multilayer perceptrons defined as $\text{Linear}(128 \to 128) \to \text{SiLU} \to \text{Dropout}(0.2) \to \text{Linear}(128 \to 1) \to \text{Softplus}$ (Fig. 9), producing positive-valued predictions $[M_{||}, D_{||}, K_{||}]$ that are consistent with their physical meaning as mass, damping, and stiffness terms.

During training, the TCN-PINN also reconstructs the interaction force $F_{\parallel}(t)$ using the predicted parameters and the observed kinematic quantities based on the mass-damper-spring model:

$$F_{\parallel}(t) = M_{\parallel}\hat{a}(t) + D_{\parallel}\hat{v}(t) + K_{\parallel}\hat{e}(t), \tag{5}$$

where $\hat{a}(t)$, $\hat{v}(t)$, and $\hat{e}(t)$ represent the measured acceleration, velocity, and displacement error projected along the interaction axis. The reconstruction error between $F_{\parallel}(t)$ and the measured force $\hat{F}(t)$ defines the physics loss, which acts as a regularization term guiding the network toward physically consistent impedance estimates.

This design allows the TCN-PINN to utilize both data-driven learning and physical laws: the TCN encoder captures temporal dependencies across EMG and kinematic signals, while the physics branch constrains the predicted parameters to obey the underlying motion-force relationship. The overall architecture, illustrated in Fig. 8, demonstrates how the learned parameters influence the reconstructed force during training, resulting in impedance estimates that are not only accurate but also physically interpretable.

Both models were implemented in PyTorch and trained using the Adam optimizer. Table I summarizes the key hyperparameter settings for both architectures. The complete implementation pipeline, including preprocessing, normalization, and data loading procedures, was developed in Python.

TABLE I
SUMMARY OF KEY HYPERPARAMETERS FOR TCN-MLP AND TCN-PINN ARCHITECTURES.

Parameter	**TCN-MLP**	**TCN-PINN**
Hidden dimension	64	128
Kernel size	3	3
Dilations	(1,2,4,8,16)	(1,2,4,8)
Normalization	BatchNorm1d	GroupNorm(1,128)
Dropout (encoder / head)	0.1 / 0.1	0.1 / 0.2
Activation	ReLU	SiLU
Batch size	64	64
Optimizer	Adam (1×10^{-3})	Adam (1×10^{-3})
Training epochs	300	300
Early stopping	30	30

II-B.2 Loss Function

Both models were trained as regression networks to estimate the endpoint impedance parameters $y_{\parallel} = [M_{\parallel}, D_{\parallel}, K_{\parallel}]$ from

multimodal temporal input data. The reference, or ground-truth, impedance values are denoted by $\hat{y} = [\hat{M}, \hat{D}, \hat{K}]$. The training objective includes a data-driven loss that enforces agreement between the predicted and measured parameters. For the TCN-PINN, an additional physics-based loss is introduced to ensure that the predictions also satisfy the dynamic mass-damper-spring relationship between motion and interaction forces. The total objective function for the physics-informed model is defined as:

$$\mathcal{L}_{\text{total}} = \mathcal{L}_{\text{data}} + \lambda \, \mathcal{L}_{\text{phys}}, \tag{6}$$

where λ is the physics-weighting coefficient, gradually increased during training with a cosine warm-up schedule, reaching $\lambda = 0.4$ at its maximum.

1. Data-driven loss

For both the TCN-MLP and TCN-PINN, the primary supervised term $\mathcal{L}_{\text{data}}$ minimizes the prediction error between the estimated parameters $y_{\|}$ and the ground-truth values $\hat{y}$. Each target component was first normalized by its median absolute value over the training set to balance the loss magnitudes across parameters with different physical scales. The data loss combines a relative Mean Absolute Error (MAE) term with a small absolute MAE contribution to improve robustness near low-magnitude regions:

$$\mathcal{L}_{\text{data}} = \sum_{i \in \{M,D,K\}} w_i \mathbb{E}\left[\alpha_i \, \frac{|y_{\|,i} - \hat{y}_i|}{|\hat{y}_i| + \epsilon} + \beta \, |y_{\|,i} - \hat{y}_i| \right], \tag{7}$$

where $\beta = 0.1$ balances the absolute MAE term and w_i are per-target weights derived from the inverse median of each parameter to prevent bias toward larger values, and $\epsilon = 10^{-6}$ is a small constant added for numerical stability. The asymmetric weighting factor α_i is defined such that $\alpha_i = \tau$ when $y_{\|,i} < \hat{y}_i$ (underestimation) and $\alpha_i = 1 - \tau$ otherwise. In this implementation, $\tau = 0.6$, so that underestimations are penalized more strongly than overestimations. Because the impedance parameters (M, D, K) differ significantly in scale and statistical distribution, a symmetric loss tends to bias the optimization toward dominant ranges. Introducing an asymmetric term mitigates this imbalance [47]. It discourages the systematic underestimation of stiffness and damping, and yields physically more plausible parameter estimates.

This data loss formulation ensures that both models learn an accurate mapping between the input features and the impedance parameters while maintaining stable gradients and balanced learning across all three outputs.

2. Physics-informed loss

The TCN-PINN introduces an additional physics-consistency term, $\mathcal{L}_{\text{phys}}$, that constrains the predicted impedance parameters to reproduce the measured interaction forces. Using the predicted parameters, the reconstructed force is compared with the measured force as defined in Equation (8). The measured force $\hat{F}(t)$ serves as the physical reference. The physics loss penalizes deviations between the reconstructed and actual forces:

$$\mathcal{L}_{\text{phys}} = \mathbb{E}_t \left[\left(\frac{F_{\|}(t) - \hat{F}(t)}{F_{\text{scale}}} \right)^2 \cdot w(t) \right], \tag{8}$$

where F_{scale} is the median of $|\hat{F}(t)|$ over the training batches to normalize the magnitude, and $w(t)$ is a normalized weighting term proportional to $|\hat{a}(t)|$, $|\hat{v}(t)|$, and $|\hat{e}(t)|$. This formulation ensures that the model focuses on regions with dynamic excitation, improving numerical stability. The inclusion of $\mathcal{L}_{\text{phys}}$ encourages the model to discover parameter combinations that not only minimize prediction error but also remain dynamically consistent with the mass-damper-spring system.

When $\lambda = 0$, the TCN-PINN reduces to the data-driven case, but the two models remain distinct in their architecture and data requirements: the TCN-MLP does not access the motion-state variables $(\hat{a}, \hat{v}, \hat{e}, \hat{F})$ used by the physics branch, thereby maintaining a separation between data-only and physics-informed learning.

II-B.3 Evaluation Metrics

The predictive performance of both models was quantitatively evaluated using three complementary metrics: the Mean Absolute Error (MAE), the normalized Mean Absolute Error (nMAE), and the coefficient of determination (R^2). These were computed for each impedance parameter, inertia (M), damping (D), and stiffness (K) on the held-out test set using unscaled values, where $\hat{y}_i$ denotes the ground-truth reference and $y_{\|,i}$ the model prediction.

1. Mean Absolute Error (MAE) and Normalized Mean Absolute Error (nMAE)

The MAE measures the average absolute deviation between the predicted and reference values:

$$\text{MAE}_i = \frac{1}{N} \sum_{n=1}^{N} \left| y_{\|,i,n} - \hat{y}_{i,n} \right|, \tag{9}$$

where $i \in \{M, D, K\}$ denotes the impedance component, and N is the total number of test samples. While MAE provides an error magnitude in physical units (kg, N·s/m, and N/m), the values of M, D, and K differ by orders of magnitude. Therefore, a normalized MAE (nMAE) was computed to enable direct comparison across parameters:

$$\text{nMAE}_i = \frac{1}{N} \sum_{n=1}^{N} \frac{\left| y_{\|,i,n} - \hat{y}_{i,n} \right|}{\text{median}(|\hat{y}_{i,\text{train}}|)} \times 100\%. \tag{10}$$

Here, the absolute error is normalized by the median magnitude of each target in the training set and expressed as a percentage. This provides a scale-invariant measure of prediction accuracy suitable for comparing performance across M, D, and K.

2. Coefficient of Determination (R^2)

The coefficient of determination quantifies how well the predicted values explain the variance of the ground-truth data:

$$R_i^2 = 1 - \frac{\sum_{n=1}^{N} \left(y_{\|,i,n} - \hat{y}_{i,n} \right)^2}{\sum_{n=1}^{N} \left(\hat{y}_{i,n} - \bar{\hat{y}}_i \right)^2}, \tag{11}$$

where $\bar{\hat{y}}_i$ is the mean of the reference target values. An R^2 value close to 1 indicates that the model accurately captures both the magnitude and variation of the true impedance parameters.

Together, these metrics provide a complete evaluation of the models: MAE and nMAE quantify prediction accuracy in physical and normalized scales, while R^2 assesses the ability to reproduce the variability and trends of the true parameters.

III Results

This section presents the results obtained from the proposed framework. Section III-A describes the results of the perturbation-based experiments, which establish the ground-truth impedance parameters and serve as reference values for training and evaluation of the neural network models. Section III-B reports the predictive performance of the proposed models, comparing the estimated impedance parameters with the identified ground-truths.

III-A Ground Truth Estimation

The reference impedance parameters were obtained from six static arm poses, each tested under two muscle activation conditions: low co-contraction (10 repetitions) and high co-contraction (5 repetitions), as well as from one dynamic trial (5 repetitions). Trials producing non-physical estimates, such as negative impedance values or perturbations with weak peak force ($F < 0.8$ N) or displacement (< 0.002 m), were discarded to ensure data quality and consistency.

In Fig. 10, the effect of muscle co-contraction is illustrated for a single arm configuration (Pose 1). Under the low co-contraction condition, the mean and standard deviation of the estimated impedance parameters along the x-, y-, and z-directions were as follows: for the x-direction, $M = 0.817 \pm 0.201$ kg, $D = 20.62 \pm 4.13$ N $\cdot$ s/m, and $K = 304.42 \pm 55.08$ N/m; for the y-direction, $M = 0.425 \pm 0.079$ kg, $D = 9.53 \pm 2.09$ N $\cdot$ s/m, and $K = 101.08 \pm 22.76$ N/m; and for the z-direction, $M = 0.368 \pm 0.072$ kg, $D = 10.66 \pm 2.17$ N $\cdot$ s/m, and $K = 195.57 \pm 23.67$ N/m.

Under high co-contraction, the impedance parameters increased noticeably, particularly along the x-direction, the principal axis of the stiffness ellipsoid for Pose 1. The estimated values were $M = 0.404 \pm 0.304$ kg, $D = 32.96 \pm 6.94$ N $\cdot$ s/m, and $K = 621.73 \pm 133.65$ N/m for x; $M = 0.363 \pm 0.099$ kg, $D = 8.86 \pm 3.18$ N $\cdot$ s/m, and $K = 297.60 \pm 72.31$ N/m for y; and $M = 0.362 \pm 0.163$ kg, $D = 18.69 \pm 5.84$ N $\cdot$ s/m, and $K = 473.74 \pm 68.26$ N/m for z.

The same figure (Fig. 10) also compares the impedance parameters between two different arm configurations (Pose 1 and Pose 5; see Fig. 2 and Fig. 6) under low co-contraction. For Pose 5, the observed values were $M = 0.243 \pm 0.128$ kg, $D = 14.08 \pm 4.95$ N $\cdot$ s/m, and $K = 219.31 \pm 42.26$ N/m in the x-direction; $M = 0.772 \pm 0.290$ kg, $D = 36.28 \pm 10.97$ N $\cdot$ s/m, and $K = 413.61 \pm 81.32$ N/m in the y-direction; and $M = 0.619 \pm 0.127$ kg, $D = 6.02 \pm 2.45$ N $\cdot$ s/m, and $K = 188.28 \pm 29.51$ N/m in the z-direction.

Impedance values were estimated for all six static poses. But, the results from Pose 1 (under two co-contraction levels) and Pose 5 (as a different arm configuration) are presented here to demonstrate the reliability of the identification procedure and the consistency of the estimated ground-truth parameters. A more detailed analysis of these results is provided in the discussion section. For the dynamic trials, mean $\pm$ standard deviation values were not reported, as both posture and muscle activation varied continuously throughout the movement, making such a summary less meaningful.

III-B Neural Network Prediction

The dataset was split into training, validation, and test sets using an 80/10/10 ratio to ensure balanced coverage of trials. Each model was trained for a maximum of 300 epochs using the Adam optimizer, with an early-stopping patience of 30 epochs to prevent overfitting.

For reference Fig. 11 shows the evolution of the total loss (Equation (6)) and physics-weighted losses ($p = \lambda \mathcal{L}_{\text{phys}}$) for the TCN-PINN ($\lambda > 0$) over epochs. Training began with total losses of $L_{\text{tr}} = 0.708$ and $L_{\text{vl}} = 0.4257$. The weighted physics-loss components, p_{tr} and p_{vl}, started near zero and gradually increased as the physics term was introduced through the warm-up schedule. After about 65 epochs, both total losses plateaued around $L_{\text{tr}} = 0.1326$ and $L_{\text{vl}} = 0.2728$, with $p_{\text{tr}} = 0.0225$ and $p_{\text{vl}} = 0.0361$. Training stopped automatically after 30 epochs, which was set as early-stopping

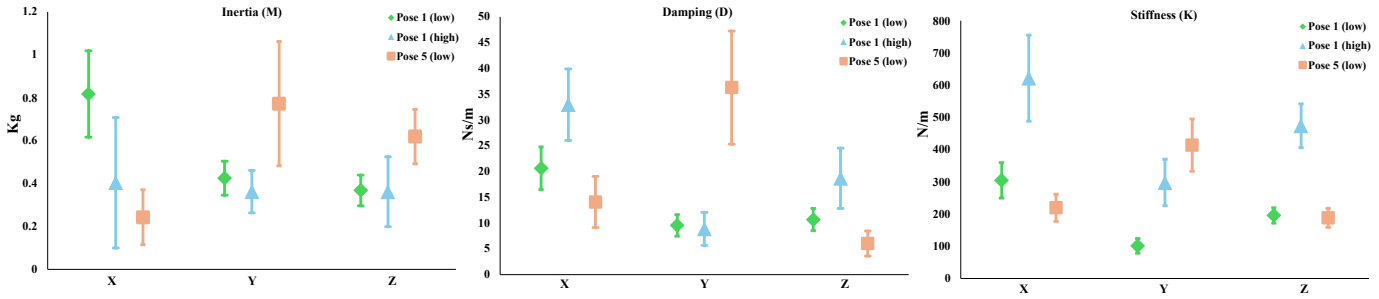

Fig. 10. Comparison of the mean ± standard deviation of the estimated impedance parameters during static trials. The panels show inertia (M), damping (D), and stiffness (K) for low and high co-contraction conditions at Pose 1, and for low contraction at Pose 5.

patience to avoid overfitting when no further improvement in validation loss is observed.

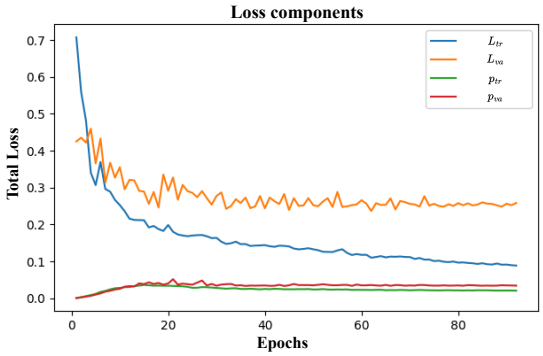

Fig. 11. Training and validation loss components over epochs.

Both models were trained using datasets consisting of static trials only and datasets combining both static and dynamic trials. Each configuration was trained and tested independently to assess the influence of data composition.

For the baseline TCN-MLP model trained on static trials only, the normalized mean absolute errors (nMAE) for inertia, damping, and stiffness were 0.380, 0.355, and 0.339, respectively, resulting in a mean nMAE of 0.358. When the dynamic trials were included, the inertia nMAE slightly decreased to 0.368, while the damping and stiffness nMAE values increased to 0.369 and 0.379, respectively, yielding a mean nMAE of 0.372.

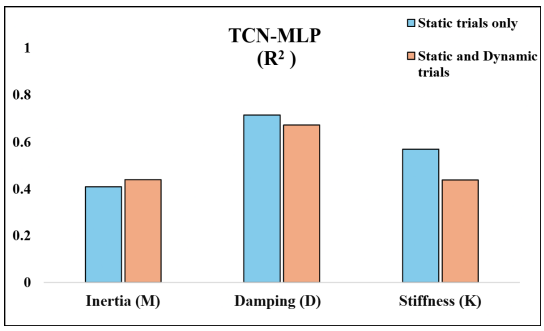

Fig. 12. Comparison of the coefficient of determination (R^2) for the TCN-MLP model trained on static trials only versus the same model trained on both static and dynamic trials.

Table II summarizes the nMAE results for all model configurations, including the TCN-PINN trained under two subcases: with the physics constraint disabled ($\lambda = 0$) and enabled ($\lambda > 0$). When trained on static trials, the TCN-PINN ($\lambda = 0$) achieved mean nMAE of 0.387, while the physics-informed TCN-PINN($\lambda > 0$) obtained 0.328. For the combined static and dynamic dataset, the corresponding mean nMAE values were 0.403 for $\lambda = 0$ and 0.328 for $\lambda > 0$.

The coefficient of determination (R^2) was also computed for all impedance components (M, D, and K). For the TCN-MLP trained on static trials, the R^2 values were 0.408, 0.714, and 0.568 for inertia, damping, and stiffness, respectively. When dynamic trials were included, the R^2 values became 0.438, 0.672, and 0.437; the comparison of these two conditions is also shown in Fig. 12.

The TCN-PINN model displayed similar trends across its two variants. For static trials, the R^2 values were 0.410, 0.444, and 0.495 when $\lambda = 0$, and 0.419, 0.636, and 0.807 for $\lambda > 0$. When trained on combined data, the R^2 values were 0.288, 0.411, and 0.389 for $\lambda = 0$, and 0.451, 0.725, and 0.747 for $\lambda > 0$. The graphical representation comparison of these four cases is presented in the Fig. 13.

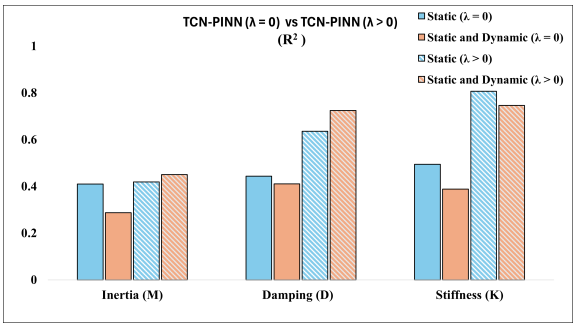

Fig. 13. Comparison of R^2 for the TCN-PINN model for both cases when the model trained on data-driven loss ($\lambda = 0$) and when physics-informed loss($\lambda > 0$) for both the static trials only and when the model was trained on both static and dynamic trials.

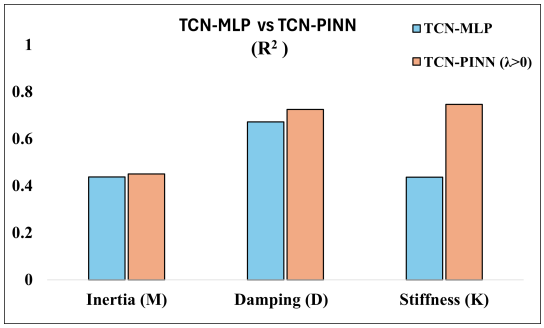

Fig. 14. Comparison of the R^2 across models.The image compares the baseline TCN-MLP and the physics-informed TCN-PINN ($\lambda > 0$) when trained on the combined dataset.

A complete comparison of R^2 values across all configurations is presented in Table II.

Lastly, the baseline TCN-MLP model was also trained for static trials only using different combinations of input modalities to evaluate the individual contribution of each modality and verify that model performance was not dominated by a single input source. The results are summarized in Table III, showing the nMAE and R^2 for each impedance parameter under various input configurations.

IV Discussion

The main objective of this work was to investigate whether incorporating physics into a data-driven model could improve the estimation of the complete human arm impedance parameters. From the results, the trend supports that including physics priors in the model strengthens the predictions, as can be interpreted from Table II.

When the TCN-PINN model was trained without the physics loss function ($\lambda = 0$), the overall evaluation metrics

TABLE II
COMPARISON OF NORMALIZED MEAN ABSOLUTE ERROR (NMAE) AND OF COEFFICIENT OF DETERMINATION (R^2) ACROSS DIFFERENT TCN-MLP AND TCN-PINN CONFIGURATIONS.

Model	**Data Type**	**M (nMAE / R^2)**	**D (nMAE / R^2)**	**K (nMAE / R^2)**	**nMAE (mean)**
TCN-MLP	Static	0.380 / 0.408	0.355 / 0.714	0.339 / 0.568	0.358
TCN-MLP	Static and Dynamic	**0.368** / 0.438	0.369 / 0.672	0.379 / 0.437	0.372
TCN-PINN($\lambda = 0$)	Static	0.377 / 0.410	0.431 / 0.444	0.352 / 0.495	0.387
TCN-PINN($\lambda > 0$)	Static	0.387 / 0.419	0.351 / 0.636	**0.246 / 0.807**	**0.328**
TCN-PINN($\lambda = 0$)	Static and Dynamic	0.388 / 0.288	0.444 / 0.411	0.377 / 0.389	0.403
TCN-PINN($\lambda > 0$)	Static and Dynamic	0.378 / **0.451**	**0.346 / 0.725**	0.261 / 0.747	**0.328**

TABLE III
COMPARISON OF INPUT FEATURE CONFIGURATIONS FOR THE BASELINE TCN-MLP MODEL, SHOWING NORMALIZED MEAN ABSOLUTE ERROR (NMAE) AND COEFFICIENT OF DETERMINATION (R^2) FOR EACH IMPEDANCE PARAMETER.

Model	**Input Features**	**M (nMAE / R^2)**	**D (nMAE / R^2)**	**K (nMAE / R^2)**	**nMAE (mean)**
TCN-MLP	Axis only	0.572 / -0.113	0.621 / 0.008	0.560 / -0.142	0.584
TCN-MLP	EMG + Axis only	0.428 / 0.287	0.499 / 0.384	0.443 / 0.336	0.456
TCN-MLP	Joint angles + Axis only	**0.344 / 0.537**	0.358 / 0.690	0.413 / 0.387	0.372
TCN-MLP	Complete (EMG + Joints + Axis)	0.380 / 0.408	**0.355 / 0.714**	**0.339 / 0.568**	**0.358**

were lower than those obtained when $\lambda > 0$. Furthermore, the model performance degraded when dynamic trials were included in training. In contrast, enabling the physics term in the loss function ($\lambda > 0$) improved impedance prediction accuracy, as illustrated in Fig. 13. Among all configurations, this physics-informed version of the TCN-PINN performed best, even when compared with the baseline TCN-MLP, which was purely data-driven (Fig. 14).

The TCN-MLP did not perform poorly overall and produced nMAE values close to the TCN-PINN with $\lambda = 0$, though it did not match the performance of the physics-informed TCN-PINN ($\lambda > 0$). The reliability of the TCN-PINN ($\lambda > 0$) can also be inferred from the model's stability when trained on combined static and dynamic trials: the model did not collapse even when dynamic data were introduced. It could be because including the dynamic trials introduces the data variability that improves the model's generalization. However, when $\lambda = 0$, including the combined dataset, the TCN-PINN performed noticeably worse. It should be noted that there were only five dynamic trials containing 90 perturbation segments, which is relatively small compared to the number of static trials. Nevertheless, these 90 dynamic perturbations introduced sufficient variability in the impedance parameters that could not be effectively captured by a purely data-driven model, a trend also observed for the TCN-MLP, though to a lesser extent. The slightly better performance of the TCN-MLP compared to the TCN-PINN without physics may arise from architectural differences between the two models.

The physics term in the loss function does not dominate the total loss and contributes to improving estimation accuracy. As seen in the results, the weighted physics loss remains smaller than the data-driven loss. Its inclusion improved model performance by integrating kinematic information and thereby helping the network maintain physically consistent predictions.

Although the TCN-PINN ($\lambda > 0$) demonstrates improved impedance estimation, its accuracy is still not sufficient for reliable real-world implementation in pHRI. This limitation is not due to a shortcoming in the network architecture itself since the training curves show no signs of underfitting or overfitting, and the mean nMAE remains below 33%. While this is not optimal, it indicates a functional baseline that can be further improved by additional hyperparameter tuning.

The main issue lies in the quality and quantity of the training data rather than the model's structure. The identification of human arm impedance parameters is a challenging problem in HRI, which depends on numerous factors, including the experimental setup, control scheme, and the biological variability between subjects, which affect the estimation. In this study, the choice of a Cartesian impedance controller was non-trivial, as most existing impedance estimation works utilize admittance or position controllers. Nevertheless, the impedance parameters identified from the perturbation experiments are comparable to estimates reported in prior literature [7], [48]. Moreover, the change in impedance characteristics of damping and stiffness parameters with a change in arm configuration and co-contraction level is as expected. The impedance gain is higher in the direction where the arm can generate greater force and stability.

The inertial parameters remain unaffected by muscle co-contraction and should remain constant for a fixed arm configuration [6]. However, in our experiments, we observed variation in the estimated inertia across different co-contraction levels for the same pose, a trend also reported in a study using endpoint impedance for skill transfer [49]. We interpret this anomaly due to estimation inaccuracy; increased endpoint stiffness due to co-contraction alters the system's motion response to perturbation, changing the timing and amplitude of the kinematic signals. This affects the conditioning of the regression in the second-order model and shifts how the model attributes force among the inertial, damping, and stiffness terms. Furthermore, inertia estimates also showed higher standard deviation compared to damping and stiffness, which aligns with findings from dynamic impedance estimation studies [48]. But in our case, this variability was

present even in static trials, which is likely due to how the Cartesian impedance controller shaped the interaction. While gravity compensation was calibrated before the experiment, some residual inertial effects from the robot's end-effector may have contributed to the observed noise in force-impulse-based estimation. Switching to an admittance controller for ground-truth identification could help improve the consistency of inertia estimates. Alternatively, adapting the robot control to stiffness and damping only during interaction may also improve efficiency and user experience [50]. In such cases, the Cartesian impedance remains a valid option for ground-truth collection due to its ability to estimate the damping and stiffness parameters and its transparent and safe behavior during pHRI.

Regarding the effect of central nervous system (CNS)-controlled modalities, the baseline TCN-MLP was trained with individual modality inputs to evaluate their relative contributions (see Table III). When trained with EMG-only or axis-only inputs, the model performed poorly compared to when joint-angle and axis information were provided together. This finding indicates that joint kinematics play a major role in impedance estimation, while including EMG data improves the estimation of damping and stiffness, highlighting the influence of muscle activation on impedance modulation. In this experiment, seven muscles were selected based on their functional roles in the chosen joint motions. However, since the co-contraction of antagonistic pairs mainly affects endpoint stiffness, targeting such muscle pairs more directly would likely improve estimation accuracy.

It should be noted that this experiment was conducted with a single subject, as the primary goal was to evaluate the feasibility of the PINN framework rather than inter-subject generalization. In future work, multi-subject datasets will be required to properly test the generalization capability of the proposed model. Additionally, joint angles in this study were estimated using marker-based tracking, which was simplified and not fully generalizable for multiple participants. For a broader study, marker placement following ISB-recommended anatomical positions [51] would provide more accurate joint angle estimates. In dynamic scenarios, however, full motion capture is often impractical outside laboratory environments. In our latest work [52], a single depth camera was successfully used to estimate joint angles and velocities in real time while interacting with a robot, proposing a more feasible solution for pHRI tasks.

Finally, it is important to acknowledge that there is no absolute ground truth for human arm impedance. All estimation methods inherently rely on assumptions and model simplifications. The true measure of an impedance estimator's usefulness lies in its practical application. With a richer and more diverse training dataset, the presented TCN-PINN model could be deployed online during physical human-robot interaction, using real-time EMG and joint data streams to estimate impedance and provide adaptive robot behavior to validate its viability.

V Conclusion

During physical human-robot interaction, humans should move naturally, engaging multiple joints without external constraints. To estimate arm endpoint impedance under such conditions, we developed a framework that combines controlled perturbation experiments for ground-truth estimation with a physics-informed, data-driven model predicting impedance from multimodal signals. The results indicate that incorporating physics priors improves prediction accuracy and physical consistency. Although not yet suitable for direct pHRI control, future work should focus on building richer training datasets, extending experiments to multiple subjects and movement conditions, and exploring real-time implementation. These developments would allow the proposed framework to evolve from an offline estimation tool into a useful foundation for adaptive, human-aware robot control.

References

[1] T. Tsuji, P. G. Morasso, K. Goto, and K. Ito, "Human hand impedance characteristics during maintained posture," *Biological cybernetics*, vol. 72, no. 6, pp. 475–485, 1995.

[2] H. Gomi and M. Kawato, "Human arm stiffness and equilibrium-point trajectory during multi-joint movement," *Biological cybernetics*, vol. 76, no. 3, pp. 163–171, 1997.

[3] E. Burdet, R. Osu, D. Franklin, T. Yoshioka, T. Milner, and M. Kawato, "A method for measuring endpoint stiffness during multi-joint arm movements," *Journal of biomechanics*, vol. 33, no. 12, pp. 1705–1709, 2000.

[4] R. D. Trumbower, M. A. Krutky, B.-S. Yang, and E. J. Perreault, "Use of self-selected postures to regulate multi-joint stiffness during unconstrained tasks," *PloS one*, vol. 4, no. 5, p. e5411, 2009.

[5] D. Lakatos, F. Petit, and P. Van Der Smagt, "Conditioning vs. excitation time for estimating impedance parameters of the human arm," in *2011 11th IEEE-RAS International Conference on Humanoid Robots*. IEEE, 2011, pp. 636–642.

[6] N. Hogan, "The Mechanics of Multi-Joint Posture and Movement Control," Tech. Rep., 1985.

[7] M. S. Erden and A. Billard, "Hand impedance measurements during interactive manual welding with a robot," *IEEE transactions on robotics*, vol. 31, no. 1, pp. 168–179, 2015.

[8] R. Wu, H. Zhang, and J. Zhao, "Robot variable impedance skill transfer and learning framework based on a simplified human arm impedance model," *IEEE Access*, vol. 8, pp. 225 627–225 638, 2020.

[9] E. Burdet, R. Osu, D. W. Franklin, T. E. Milner, and M. Kawato, "The central nervous system stabilizes unstable dynamics by learning optimal impedance," *Nature*, vol. 414, no. 6862, pp. 446–449, 2001.

[10] A. Weiss, A.-K. Wortmeier, and B. Kubicek, "Cobots in industry 4.0: A roadmap for future practice studies on human–robot collaboration," *IEEE Transactions on Human-Machine Systems*, vol. 51, no. 4, pp. 335–345, 2021.

[11] F. J. Abu-Dakka and M. Saveriano, "Variable impedance control and learning – A review," 10 2020. [Online]. Available: http://arxiv.org/abs/2010.06246http://dx.doi.org/10.3389/frobt.2020.590681

[12] C. Fang, L. Peternel, A. Seth, M. Sartori, K. Mombaur, and E. Yoshida, "Human Modeling in Physical Human-Robot Interaction: A Brief Survey," *IEEE Robotics and Automation Letters*, vol. 8, no. 9, pp. 5799–5806, 9 2023.

[13] L. Peternel, N. Tsagarakis, and A. Ajoudani, "Towards multi-modal intention interfaces for human-robot co-manipulation," in *2016 IEEE/RSJ international conference on intelligent robots and systems (IROS)*. IEEE, 2016, pp. 2663–2669.

[14] ——, "A human-robot co-manipulation approach based on human sensorimotor information," *IEEE Transactions on Neural Systems and Rehabilitation Engineering*, vol. 25, no. 7, pp. 811–822, 7 2017.

[15] Z. Wang, H. Xu, R. Jiang, Y. Zhou, S. Jiang, X. Cheng, X. Li, and B. He, "Adaptive variable impedance control in physical human-robot

interaction based on arm end stiffness estimation," *IEEE Transactions on Instrumentation and Measurement*, 2025.

[16] M. S. Erden and A. Billard, "End-point impedance measurements across dominant and nondominant hands and robotic assistance with directional damping," *IEEE Transactions on Cybernetics*, vol. 45, no. 6, pp. 1146–1157, 6 2015.

[17] F. A. Mussa-Ivaldi, N. Hogan, and E. Bizzi, "Neural, mechanical, and geometric factors subserving arm posture in humans," *Journal of neuroscience*, vol. 5, no. 10, pp. 2732–2743, 1985.

[18] P. K. Artemiadis, P. T. Katsiaris, M. V. Liarokapis, and K. J. Kyriakopoulos, "Human arm impedance: Characterization and modeling in 3d space," in *2010 IEEE/RSJ international conference on intelligent robots and systems*. IEEE, 2010, pp. 3103–3108.

[19] T. Flash and F. Mussa-Ivaldi, "Human arm stiffness characteristics during the maintenance of posture," *Experimental brain research*, vol. 82, no. 2, pp. 315–326, 1990.

[20] P. K. Artemiadis and K. J. Kyriakopoulos, "An EMG-based robot control scheme robust to time-varying EMG signal features," *IEEE Transactions on Information Technology in Biomedicine*, vol. 14, no. 3, pp. 582–588, 5 2010.

[21] E. J. Perreault, R. F. Kirsch, and P. E. Crago, "Multijoint dynamics and postural stability of the human arm," *Experimental brain research*, vol. 157, no. 4, pp. 507–517, 2004.

[22] ——, "Voluntary control of static endpoint stiffness during force regulation tasks," *Journal of neurophysiology*, vol. 87, no. 6, pp. 2808–2816, 2002.

[23] D. Lakatos, D. Rüschen, J. Bayer, J. Vogel, and P. van der Smagt, "Identification of human limb stiffness in 5 dof and estimation via emg," in *Experimental Robotics: The 13th International Symposium on Experimental Robotics*. Springer, 2013, pp. 89–99.

[24] C. Fang, A. Ajoudani, A. Bicchi, and N. G. Tsagarakis, "Online Model Based Estimation of Complete Joint Stiffness of Human Arm," Tech. Rep.

[25] R. Osu and H. Gomi, "Multijoint muscle regulation mechanisms examined by measured human arm stiffness and emg signals," *Journal of neurophysiology*, vol. 81, no. 4, pp. 1458–1468, 1999.

[26] A. Ajoudani, N. Tsagarakis, and A. Bicchi, "Tele-impedance: Teleoperation with impedance regulation using a body–machine interface," *The International Journal of Robotics Research*, vol. 31, no. 13, pp. 1642–1656, 2012.

[27] A. Ajoudani, C. Fang, N. Tsagarakis, and A. Bicchi, "Reduced-complexity representation of the human arm active endpoint stiffness for supervisory control of remote manipulation," *The International Journal of Robotics Research*, vol. 37, no. 1, pp. 155–167, 2018.

[28] Y. Wu, F. Zhao, W. Kim, and A. Ajoudani, "An intuitive formulation of the human arm active endpoint stiffness," *Sensors (Switzerland)*, vol. 20, no. 18, pp. 1–15, 9 2020.

[29] M. Farajtabar and M. Charbonneau, "The path towards contact-based physical human–robot interaction," *Robotics and Autonomous Systems*, vol. 182, 12 2024.

[30] H. K. Kim, B. Kang, B. Kim, and S. Park, "Estimation of multijoint stiffness using electromyogram and artificial neural network," *IEEE Transactions on Systems, Man, and Cybernetics Part A:Systems and Humans*, vol. 39, no. 5, pp. 972–980, 2009.

[31] Y. Ma, Q. Liu, H. Liu, and W. Meng, "sEMG-Based Estimation of Human Arm Endpoint Stiffness Using Long Short-Term Memory Neural Networks and Autoencoders," in *Lecture Notes in Computer Science (including subseries Lecture Notes in Artificial Intelligence and Lecture Notes in Bioinformatics)*, vol. 13456 LNAI. Springer Science and Business Media Deutschland GmbH, 2022, pp. 699–710.

[32] J. Zhang, Y. Zhao, F. Shone, Z. Li, A. F. Frangi, S. Q. Xie, and Z. Q. Zhang, "Physics-Informed Deep Learning for Musculoskeletal Modeling: Predicting Muscle Forces and Joint Kinematics From Surface EMG," *IEEE Transactions on Neural Systems and Rehabilitation Engineering*, vol. 31, pp. 484–493, 2023.

[33] M. Raissi, P. Perdikaris, and G. E. Karniadakis, "Physics-informed neural networks: A deep learning framework for solving forward and inverse problems involving nonlinear partial differential equations," *Journal of Computational physics*, vol. 378, pp. 686–707, 2019.

[34] A. Farea, O. Yli-Harja, and F. Emmert-Streib, "Understanding physics-informed neural networks: techniques, applications, trends, and challenges," *AI*, vol. 5, no. 3, pp. 1534–1557, 2024.

[35] R. Kumar, S. P. Muthukrishnan, L. Kumar, and S. Roy, "Predicting multi-joint kinematics of the upper limb from emg signals across varied loads with a physics-informed neural network," *arXiv preprint arXiv:2312.09418*, 2023.

[36] H. Tugal, B. Gautier, M. Kircicek, and M. S. Erden, "Hand-impedance measurement during laparoscopic training coupled with robotic manipulators," in *2018 IEEE/RSJ International Conference on Intelligent Robots and Systems (IROS)*. IEEE, 2018, pp. 4404–4410.

[37] Y. Wu, F. Zhao, W. Kim, and A. Ajoudani, "An intuitive formulation of the human arm active endpoint stiffness," *Sensors*, vol. 20, no. 18, p. 5357, 2020.

[38] S. P. Buerger and N. Hogan, "Complementary stability and loop shaping for improved human–robot interaction," *IEEE Transactions on Robotics*, vol. 23, no. 2, pp. 232–244, 2007.

[39] H. J. Hermens, B. Freriks, C. Disselhorst-Klug, and G. Rau, "Development of recommendations for semg sensors and sensor placement procedures," *Journal of electromyography and Kinesiology*, vol. 10, no. 5, pp. 361–374, 2000.

[40] A. Ajoudani, A. M. Zanchettin, S. Ivaldi, A. Albu-Schäffer, K. Kosuge, and O. Khatib, "Progress and prospects of the human–robot collaboration," *Autonomous robots*, vol. 42, pp. 957–975, 2018.

[41] H. Börner, S. Endo, and S. Hirche, "Estimation of involuntary components of human arm impedance in multi-joint movements via feedback jerk isolation," *Frontiers in Neuroscience*, vol. 14, p. 459, 2020.

[42] E. Burdet, R. Osu, D. W. Franklin, T. Yoshioka, T. E. Milner, and M. Kawato, "A method for measuring endpoint sti!ness during multi-joint arm movements," Tech. Rep., 2000.

[43] P. Konrad, *The ABC of EMG: A Practical Introduction to Kinesiological Electromyography*, Noraxon USA, Inc., Apr. 2005, version 1.0.

[44] E. de Vlugt, A. C. Schouten, F. C. van der Helm, P. C. Teerhuis, and G. G. Brouwn, "A force-controlled planar haptic device for movement control analysis of the human arm," *Journal of neuroscience methods*, vol. 129, no. 2, pp. 151–168, 2003.

[45] D. W. Franklin and D. M. Wolpert, "Computational mechanisms of sensorimotor control," *Neuron*, vol. 72, no. 3, pp. 425–442, 2011.

[46] S. Bai, J. Z. Kolter, and V. Koltun, "An empirical evaluation of generic convolutional and recurrent networks for sequence modeling," *arXiv preprint arXiv:1803.01271*, 2018.

[47] J. Terven, D.-M. Cordova-Esparza, J.-A. Romero-González, A. Ramírez-Pedraza, and E. Chávez-Urbiola, "A comprehensive survey of loss functions and metrics in deep learning," *Artificial Intelligence Review*, vol. 58, no. 7, p. 195, 2025.

[48] V. Fortineau, M. Makarov, P. Rodriguez-Ayerbe, and I. A. Siegler, "Towards a seamless experimental protocol for human arm impedance estimation in an interactive dynamic task," in *2021 30th IEEE International Conference on Robot and Human Interactive Communication, RO-MAN 2021*. Institute of Electrical and Electronics Engineers Inc., 8 2021, pp. 31–36.

[49] R. Wu, H. Zhang, and J. Zhao, "Robot Variable Impedance Skill Transfer and Learning Framework Based on a Simplified Human Arm Impedance Model," *IEEE Access*, vol. 8, pp. 225 627–225 638, 2020.

[50] F. Zahedi and H. Lee, "Biomechanics-based user-adaptive variable impedance control for enhanced physical human–robot interaction using bayesian optimization," *Advanced Intelligent Systems*, vol. 7, no. 2, p. 2400333, 2025.

[51] G. Wu, F. C. Van Der Helm, H. E. Veeger, M. Makhsous, P. Van Roy, C. Anglin, J. Nagels, A. R. Karduna, K. McQuade, X. Wang, F. W. Werner, and B. Buchholz, "ISB recommendation on definitions of joint coordinate systems of various joints for the reporting of human joint motion - Part II: Shoulder, elbow, wrist and hand," *Journal of Biomechanics*, vol. 38, no. 5, pp. 981–992, 5 2005.

[52] Y. Hu, A. Srivastava, L. Peternel, and J. M. Prendergast, "Fusing physical hri with rgb-d skeleton tracking for improved human arm pose estimation," Delft, The Netherlands, 2025, under review.

Appendix A

Experiment Protocol and Procedure

The purpose of this experiment is to collect data during physical human-robot interaction, where the participant performs a collaborative task with the robot by holding its end effector. The data collected include the electromyographic (EMG) activity of major arm muscles contributing to mobility, joint motion kinematics via a marker-based motion capture system, and force/torque measurements at the human-robot contact point obtained from a load cell attached to the robot's end effector. This multimodal dataset is used as input to a machine-learning model designed to estimate the human arm endpoint stiffness during collaboration.

V-A Apparatus and Their Purpose

- **OptiTrack Prime 13W** (NaturalPoint Inc., Corvallis, OR, USA): Captures the motion of the participant during the experiment.
- **Bota Systems SENSONE** (Bota Systems AG, Zürich, Switzerland): 6-axis force-torque sensor measuring interaction forces and torques at the robot's end effector.
- **Trigno Wireless Biofeedback System** (Delsys Inc., Natick, MA, USA): Surface electromyography (sEMG) system for recording muscle activity throughout the experiment.
- **KUKA LBR iiwa 7** (KUKA AG, Augsburg, Germany): 7-degree-of-freedom collaborative robot used to perform the physical interaction task.
- **Manipulation rod**: Attached to the robot's end effector to allow a comfortable grasp and manipulation.
- **Wrist brace**: Restricts wrist movement and ensures consistent arm posture across trials.

Estimated duration: approximately 3-3.5 h per participant.

V-B Step 1: Participant Preparation and Information Collection (Est. $<$ 10 min)

Participants are instructed to wear a non-reflective, tight-fitting athletic shirt or tank top to ensure stable EMG and marker placement. Placement always prioritizes participant comfort and privacy.

1) Explain the procedure clearly to the participant.
2) Provide and collect the signed informed-consent form.
3) Record demographic and biometric information:
   - Participant ID, age, sex, height, and weight.
   - Dominant hand (only right-handed interaction is conducted).
   - Note any musculoskeletal issues, injuries, or skin sensitivities.

V-C Step 2: EMG Sensor Placement and MVIC Collection (Est. $\sim$30-35 min)

Before the main task, maximum muscle activation is measured using Maximum Voluntary Isometric Contraction (MVIC) tests. Seven dominant muscles are selected to capture the activity contributing to the arm's five degrees of freedom (DoF): three at the shoulder, one at the elbow, and one at the forearm.

Functional Degrees of Freedom

1) Shoulder extension/flexion
2) Shoulder abduction/adduction
3) Shoulder internal/external rotation
4) Elbow flexion/extension
5) Forearm pronation/supination

Muscles Monitored

1) **Biceps Brachii**: Mid-belly placement, one-third from cubital fossa to acromion [5]. Starting posture: seated, elbow flexed 90°, forearm horizontal, palm up. MVIC task: lift an immovable object or push upward against resistance.

2) **Triceps Brachii (Long Head)**: On the muscle belly, halfway between posterior acromion and olecranon, offset medially by two finger-widths [5]. Starting posture: shoulder 90° abduction, elbow 90° flexed, palm down. MVIC task: push outward/extend against resistance (3-5 s).
3) **Pronator Teres**: Volar side of the upper forearm, 3 cm distal to the midpoint between the medial epicondyle and biceps tendon [1]. MVIC task: elbow 90°, wrist straight, forearm neutral; pronate against manual resistance without gripping.
4) **Anterior Deltoid**: 3.5 cm below and anterior to the acromion, along the line toward the thumb [5]. Starting posture: sitting, arms hanging vertically, palms inward. MVIC task: shoulder flexion 45° with resistance at the wrist [3].
5) **Middle Deltoid**: 3 cm below the acromion on the lateral mid-deltoid, aligned from the acromion to the lateral epicondyle [5]. Starting posture: sitting upright, stabilized trunk and scapula. MVIC task: shoulder abduction 45° with resistance at the wrist [3].
6) **Posterior Deltoid**: Two fingerbreadths posterior to the acromion, oriented toward the little finger [5]. Starting posture: erect sitting, arms vertical, palms inward. MVIC task: shoulder horizontal extension with resistance at the elbow [3].
7) **Pectoralis Major**: Clavicular portion, 3.5 cm medial to the anterior axillary line [2]. MVIC task: shoulder 90°, elbow 90°, bilateral palm press against resistance [3].

MVIC Trial Structure:

- Three repetitions per muscle
- Each contraction lasts 3-5 s
- 1-2 min rest between repetitions
- Monitor for fatigue or discomfort; provide extra rest if needed
- Participants may decline any painful trial

Sites are shaved and cleaned with isopropyl alcohol before placement. Adhesive interfaces are single-use.

Caution: Do not use electrodes on participants with silver allergies. Discontinue immediately if irritation occurs and document any reaction.

V-D Step 3: Marker Placement for Joint-Angle Capture (Est. ∼10 min)

Three rigid bodies are tracked to capture upper-limb kinematics:

1) Shoulder
2) Upper arm
3) Forearm

After placement, participants stand in the calibrated OptiTrack volume in a neutral reference position to record baseline pose.

V-E Step 4: Main Perturbation Experiment (Est. ≈ 2 h)

Perturbation testing includes both static and dynamic conditions. Force/torque data and end-effector pose are recorded at 1000 Hz and 200 Hz, respectively. The robot operates in Cartesian-impedance control mode:

- $K_{\text{vir}} \approx 0$ N/m
- D_{vir} ratio $= 0.9$
- $M_{\text{vir}} \approx 0$ kg

Coordinate-Frame Definition:

1) x-axis: shortest side of OptiTrack CS-200 calibration tool
2) z-axis: longest side
3) y-axis: $\mathbf{y} = \mathbf{z} \times \mathbf{x}$

Neural-network input segments correspond to 0-260 ms after perturbation onset. All devices are synchronized via Network Time Protocol (NTP):

- Linux computer as master clock.
- OptiTrack (Windows 10) and EMG source (Windows 11) synchronized to the master.

Static Postures

Each static trial lasts 90 s:

- 2 s baseline
- 18 perturbations ($\geq$ 4 s apart)
- 4 s final settling period

Postures:

1) **Neutral:** Shoulder $\approx 0^\circ$ flexion/abduction; elbow $\approx 90^\circ$; forearm neutral.
2) **Flexed shoulder, neutral elbow:** Shoulder $\approx 90^\circ$ flexion; elbow neutral; forearm neutral.
3) **Partial forward extension:** Shoulder ≈ 75–90° flexion; elbow partially extended; forearm neutral.
4) **Abducted shoulder:** Shoulder $\approx 90^\circ$ abduction and internal rotation; elbow neutral; forearm neutral.
5) **Inward shoulder extension:** Shoulder adducted and internally rotated; elbow extended; forearm neutral.
6) **Outward shoulder extension:** Shoulder abducted and externally rotated; elbow extended; forearm neutral.

Each posture is maintained rigidly during perturbations.

Rest intervals: 1 min after every 3 trials; 3 min between posture blocks; 5 min between static and dynamic sections.

Dynamic Movement Patterns

Each dynamic trial lasts 90 s with 18 perturbations perpendicular to the motion direction. Participants may follow a reference trajectory while reacting naturally to perturbations.

Patterns:

- X-directional motion
- Y-directional motion
- Z-directional motion

Contraction Levels:

- Relaxed: < 0.1 % CIC
- High: > 0.1 % CIC

Contraction emphasis is on the elbow (biceps and triceps), as prior research indicates that combined activation of these muscles explains 76-89 % of stiffness-ellipsoid variance across co-contraction levels [4].

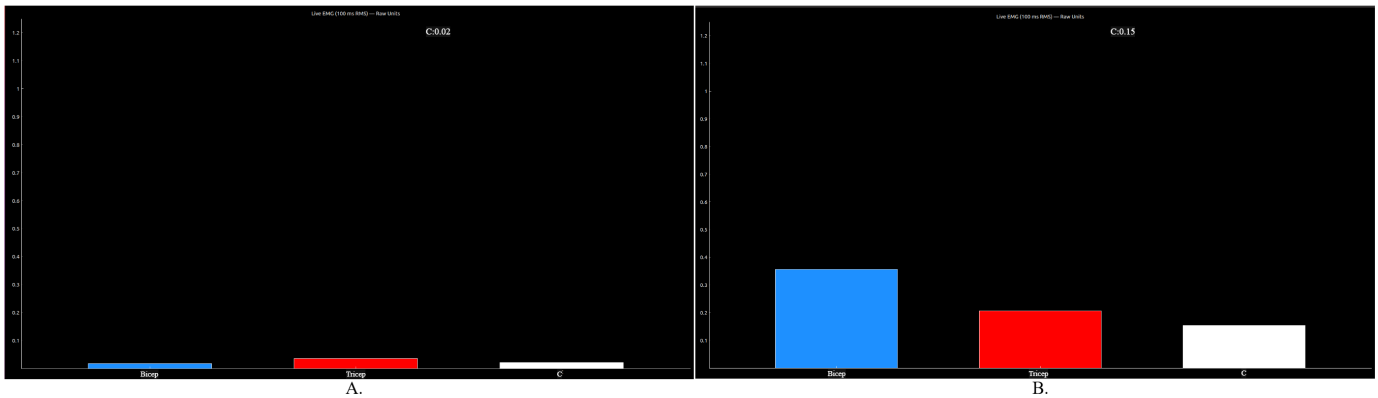

A. B.

Fig. 15. Visual cues provided to help participants maintain consistent contraction levels during the task.

References

[1] A. P. Abraham *et al.*, "Surface electromyography activity in the upper limbs of patients following surgery for compressive cervical myelopathy," *Neurology India*, vol. 63, no. 6, pp. 903-910, 2015.

[2] H. Król, G. Sobota, and A. Nawrat, "Effect of electrode position on EMG recording in pectoralis major," *Journal of Human Kinetics*, vol. 17, pp. 105-112, 2007.

[3] C. E. Boettcher, K. A. Ginn, and I. Cathers, "Standard maximum isometric voluntary contraction tests for normalizing shoulder muscle EMG," *Journal of Orthopaedic Research*, vol. 26, no. 12, pp. 1591-1597, 2008.

[4] A. Ajoudani, C. Fang, N. Tsagarakis, and A. Bicchi, "Reduced-complexity representation of the human arm active endpoint stiffness for supervisory control of remote manipulation," *International Journal of Robotics Research*, vol. 37, no. 1, pp. 155-167, 2018.

[5] H. J. Hermens, B. Freriks, C. Disselhorst-Klug, and G. Rau, "Development of recommendations for sEMG sensors and sensor placement procedures," *Journal of Electromyography and Kinesiology*, vol. 10, no. 5, pp. 361-374, 2000.

Appendix B

Ground Truth

This appendix presents the mean ± standard deviation of ground-truth endpoint impedance parameters;inertia M (kg), damping D (N·s/m), and stiffness K (N/m)for six arm configurations (Pose 1-6) under low and high co-contraction.

Pose 1

Low Co-contraction

Axis	M **(kg)**	D **(N·s/m)**	K **(N/m)**
X	0.817 ± 0.201	20.62 ± 4.13	304.42 ± 55.08
Y	0.425 ± 0.079	9.53 ± 2.09	101.08 ± 22.76
Z	0.368 ± 0.072	10.66 ± 2.17	195.57 ± 23.67

TABLE IV
POSE 1 : LOW CO-CONTRACTION.

High Co-contraction

Axis	M **(kg)**	D **(N·s/m)**	K **(N/m)**
X	0.404 ± 0.304	32.96 ± 6.94	621.73 ± 133.65
Y	0.363 ± 0.199	8.86 ± 3.18	297.60 ± 72.31
Z	0.362 ± 0.163	18.69 ± 5.84	473.74 ± 68.26

TABLE V
POSE 1 : HIGH CO-CONTRACTION.

Pose 2

Low Co-contraction

Axis	M **(kg)**	D **(N·s/m)**	K **(N/m)**
X	0.433 ± 0.145	8.02 ± 3.41	202.95 ± 56.09
Y	1.015 ± 0.233	21.21 ± 3.86	144.73 ± 42.74
Z	0.470 ± 0.112	5.92 ± 2.58	247.79 ± 31.29

TABLE VI
POSE 2 : LOW CO-CONTRACTION.

High Co-contraction

Axis	M (kg)	D (N·s/m)	K (N/m)
X	0.277 ± 0.143	14.69 ± 5.55	557.64 ± 97.20
Y	0.990 ± 0.239	21.83 ± 5.36	232.81 ± 80.44
Z	0.470 ± 0.174	9.17 ± 3.73	308.90 ± 40.57

TABLE VII
POSE 2 : HIGH CO-CONTRACTION.

Pose 3

Low Co-contraction

Axis	M (kg)	D (N·s/m)	K (N/m)
X	0.576 ± 0.172	18.66 ± 5.20	398.71 ± 68.52
Y	0.480 ± 0.110	7.88 ± 2.60	136.86 ± 33.24
Z	0.668 ± 0.120	7.41 ± 2.64	204.21 ± 37.79

TABLE VIII
POSE 3 : LOW CO-CONTRACTION.

High Co-contraction

Axis	M (kg)	D (N·s/m)	K (N/m)
X	0.354 ± 0.302	28.55 ± 7.74	874.79 ± 88.78
Y	0.546 ± 0.137	7.24 ± 2.25	221.83 ± 31.55
Z	0.690 ± 0.224	8.53 ± 4.03	349.93 ± 59.89

TABLE IX
POSE 3 : HIGH CO-CONTRACTION.

Pose 4

Low Co-contraction

Axis	M (kg)	D (N·s/m)	K (N/m)
X	1.082 ± 0.345	14.18 ± 5.68	261.45 ± 64.84
Y	0.290 ± 0.068	6.59 ± 1.68	168.20 ± 23.54
Z	0.373 ± 0.100	10.69 ± 2.65	189.71 ± 36.64

TABLE X
POSE 4 : LOW CO-CONTRACTION.

High Co-contraction

Axis	M (kg)	D (N·s/m)	K (N/m)
X	0.926 ± 0.516	23.63 ± 9.94	374.35 ± 118.94
Y	0.092 ± 0.073	9.74 ± 1.85	412.50 ± 99.38
Z	0.535 ± 0.278	5.71 ± 3.47	364.28 ± 64.19

TABLE XI
POSE 4 : HIGH CO-CONTRACTION.

Pose 5

Low Co-contraction

Axis	M (kg)	D (N·s/m)	K (N/m)
X	0.243 ± 0.127	14.08 ± 4.95	219.31 ± 42.34
Y	0.772 ± 0.291	36.28 ± 10.99	413.61 ± 81.41
Z	0.619 ± 0.127	6.01 ± 2.45	188.28 ± 29.46

TABLE XII
POSE 5 : LOW CO-CONTRACTION.

High Co-contraction

Axis	M (kg)	D (N·s/m)	K (N/m)
X	0.102 ± 0.057	32.58 ± 4.72	307.02 ± 23.44
Y	0.687 ± 0.494	57.00 ± 18.22	644.19 ± 291.12
Z	0.758 ± 0.247	4.80 ± 2.82	304.08 ± 66.92

TABLE XIII
POSE 5 : HIGH CO-CONTRACTION.

Pose 6

Low Co-contraction

Axis	M (kg)	D (N·s/m)	K (N/m)
X	0.301 ± 0.135	23.67 ± 5.92	97.29 ± 51.09
Y	0.185 ± 0.153	34.94 ± 7.12	531.02 ± 98.43
Z	0.707 ± 0.101	5.25 ± 2.29	187.09 ± 30.27

TABLE XIV
POSE 6 : LOW CO-CONTRACTION.

High Co-contraction

Axis	M (kg)	D (N·s/m)	K (N/m)
X	0.599 ± 0.420	33.96 ± 8.89	188.80 ± 96.72
Y	$0.139 \pm 0.000^{*}$	$28.47 \pm 0.000^{*}$	$1282.18 \pm 0.000^{*}$
Z	0.670 ± 0.340	3.46 ± 3.23	262.35 ± 52.12

* Zero standard deviation indicates that, after quality control, only a single window remained for this axis. Windows with implausible values were discarded using the following quality check (QC) gates: any $M, D, K < 0$, peak force $F < 0.8$ N, or peak displacement < 0.002 m.

TABLE XV
POSE 6 : HIGH CO-CONTRACTION.

V-F Dynamic Trial Signals

This section presents the representative signals recorded during a dynamic trial. The signals include commanded force impulses, end-effector position, velocity, acceleration, and measured interaction force. Each plot shows the three Cartesian axes (x, y, z). Together, these illustrate how short-duration force impulses elicit measurable end-effector displacements and dynamic responses that form the basis for impedance estimation.

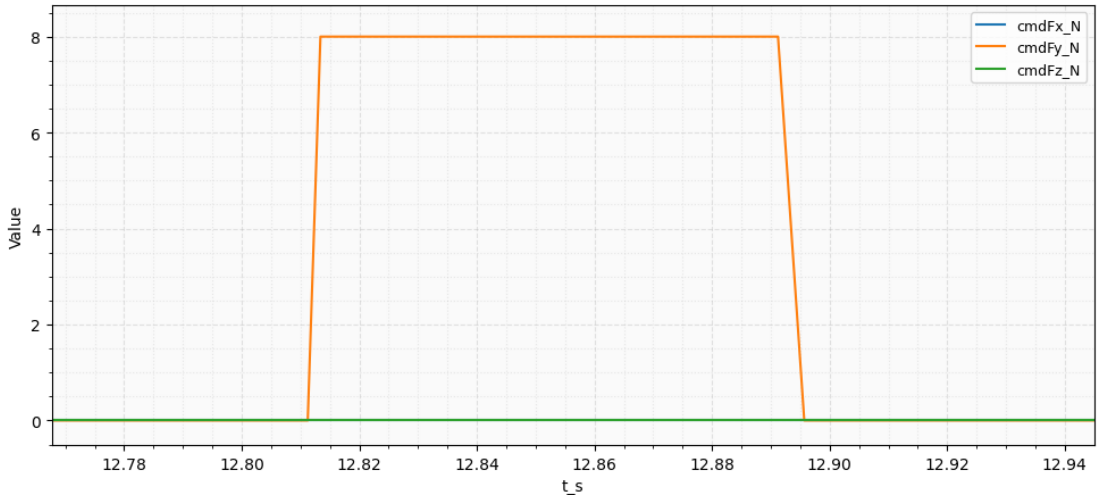

Fig. 16. Commanded force impulses ($\mathbf{F}_{cmd}$) along the Cartesian axes. Each rectangular pulse represents a 80 ms perturbation applied through the Cartesian impedance controller. The impulses are spaced by several seconds to allow the system to return to steady state between perturbations.

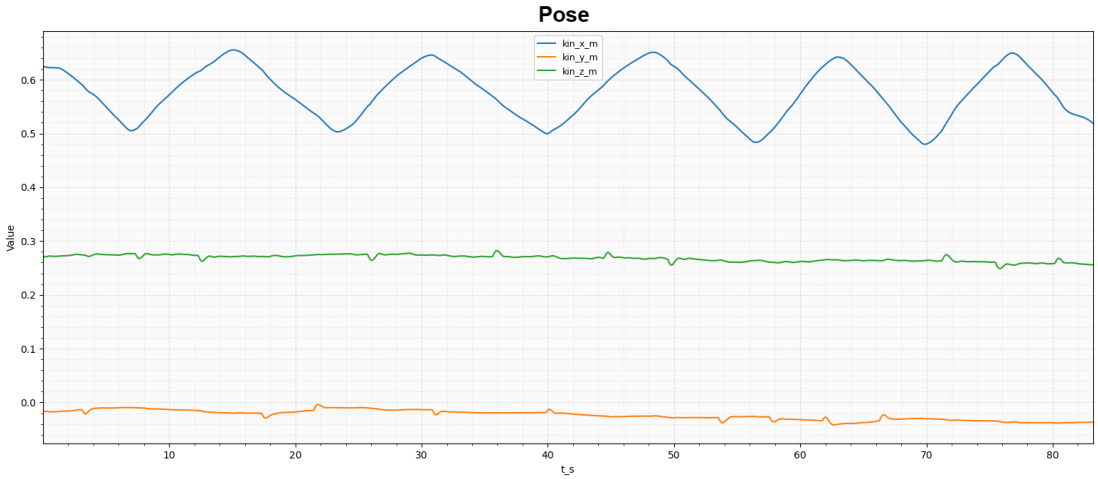

Fig. 17. End-effector position ($\mathbf{x}(t)$) along x, y, and z axes during dynamic movement. The smooth oscillatory profile in x indicates the imposed trajectory, while the other axes remain nearly constant except when perturbed.

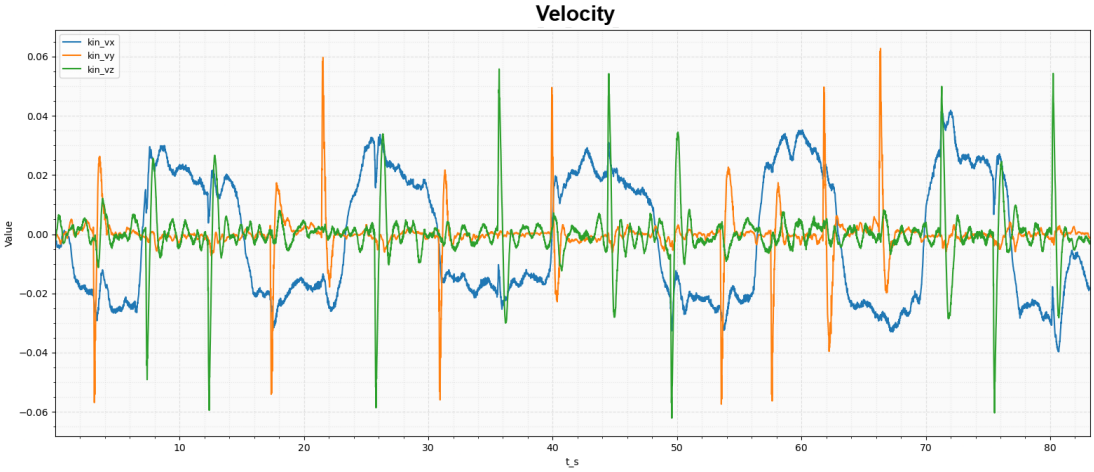

Fig. 18. End-effector velocity ($\dot{\mathbf{x}}(t)$) during the dynamic task. Distinct transient peaks correspond to the short force impulses, while the baseline oscillations reflect the voluntary cyclic motion.

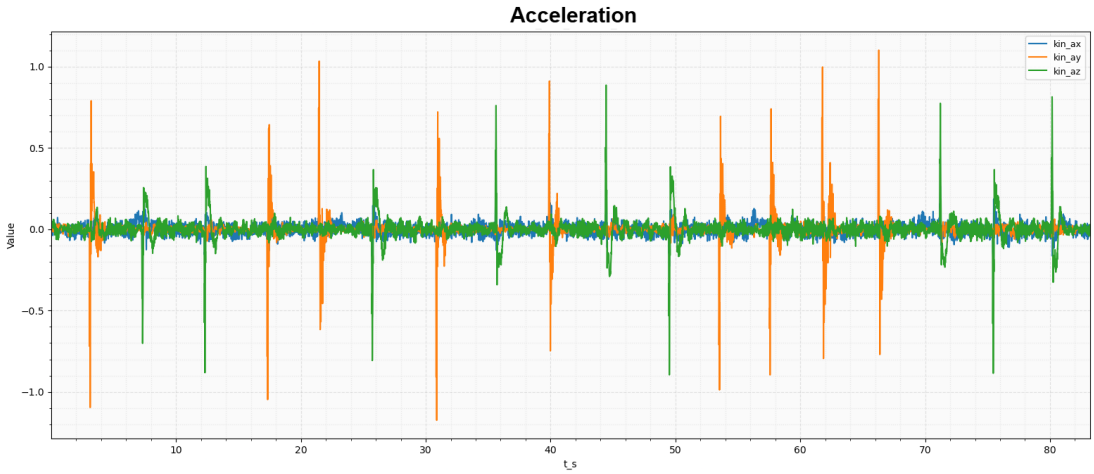

Fig. 19. End-effector acceleration ($\ddot{\mathbf{x}}(t)$) estimated from filtered position data. Acceleration spikes align closely with the timing of each commanded impulse, confirming proper temporal synchronization and dynamic responsiveness.

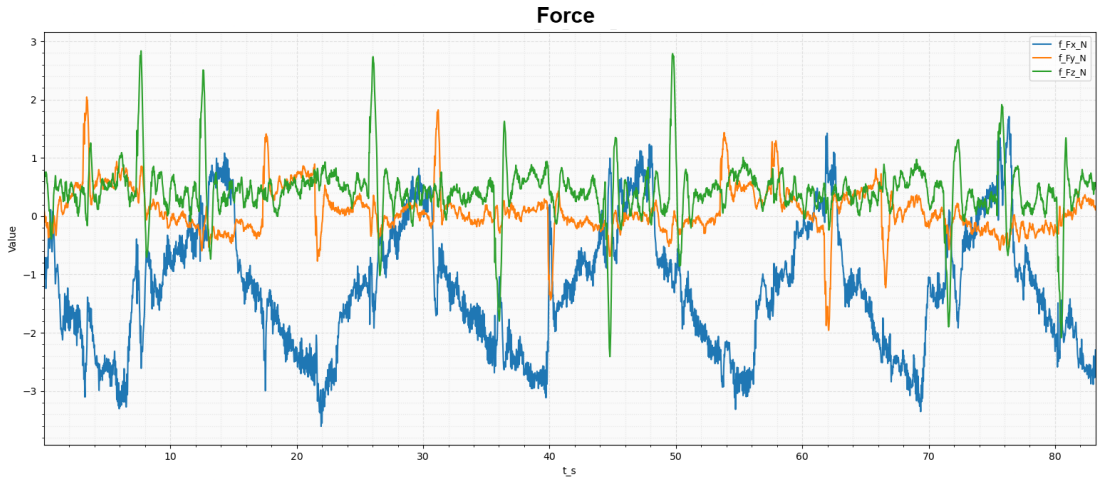

Fig. 20. Measured interaction force ($\mathbf{F}_{meas}$) recorded from the force/torque sensor. Each impulse produces a sharp increase in the corresponding force direction, followed by a damped response reflecting the coupled human-robot dynamics.

Appendix C

Neural Network Supplementary Results

This appendix presents additional results from the neural network training and evaluation. The goal is to show the learning behavior of all trained models.

Figure 21 and 22 show the loss curves for each model variant used in this study. Across all configurations, the training and validation losses converge smoothly without divergence, indicating stable optimization and no signs of overfitting or underfitting. This confirms that the networks can generalize well within the available dataset.

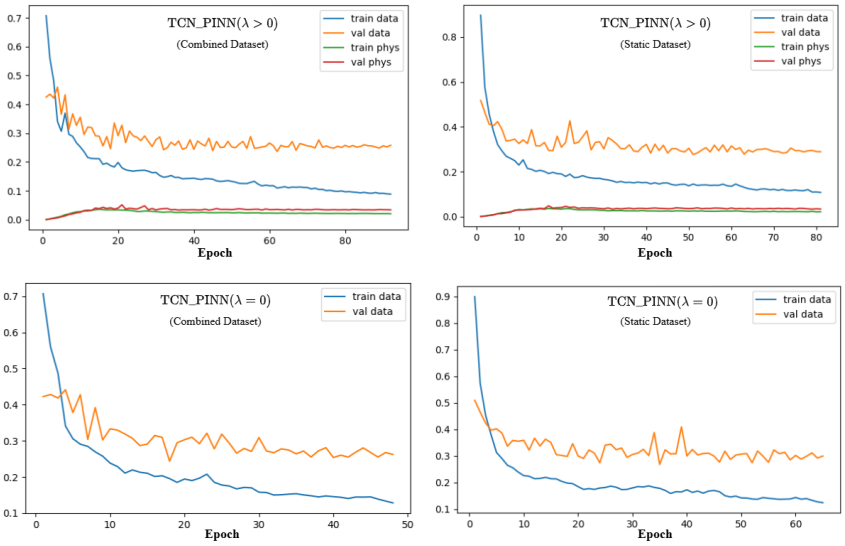

Fig. 21. Loss curves for the TCN-PINN for all scenarios.

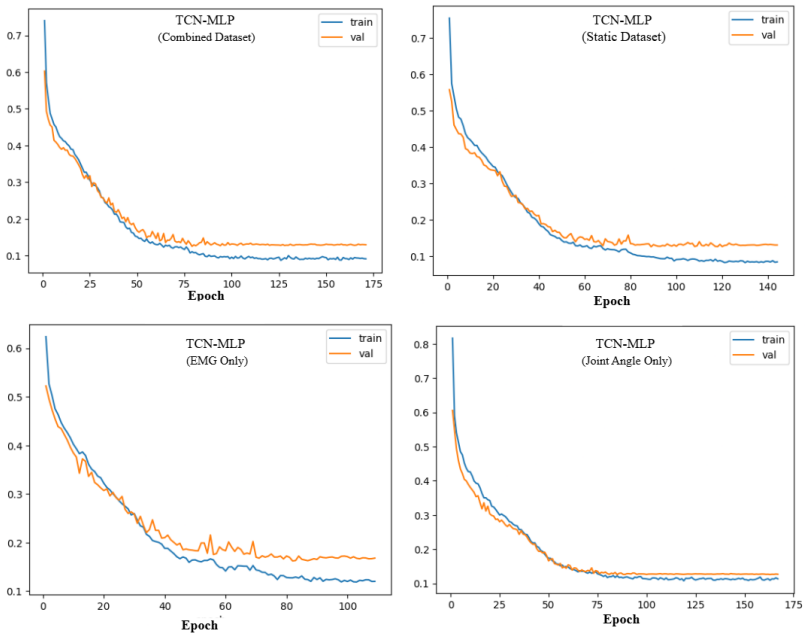

Fig. 22. Loss curve for TCN-MLP under different input configurations..

Figure 23 compares the parity plots of the physics-informed model (TCN-PINN, $\lambda > 0$) and its non-physics counterpart (TCN-PINN, $\lambda = 0$) for the predicted impedance parameters i.e inertia (M), damping (D), and stiffness (K). Each scatter plot shows the relationship between the predicted and true values, where points closer to the diagonal line indicate higher prediction accuracy. The physics-informed model demonstrates a tighter clustering along the identity line, particularly for D and K, indicating improved consistency and reduced bias when physical constraints are incorporated into the learning objective. This visual comparison supports the quantitative results, confirming that embedding physics priors improves the model's ability to produce physically plausible and accurate impedance estimates, especially in high co-contraction conditions where impedance values are higher.

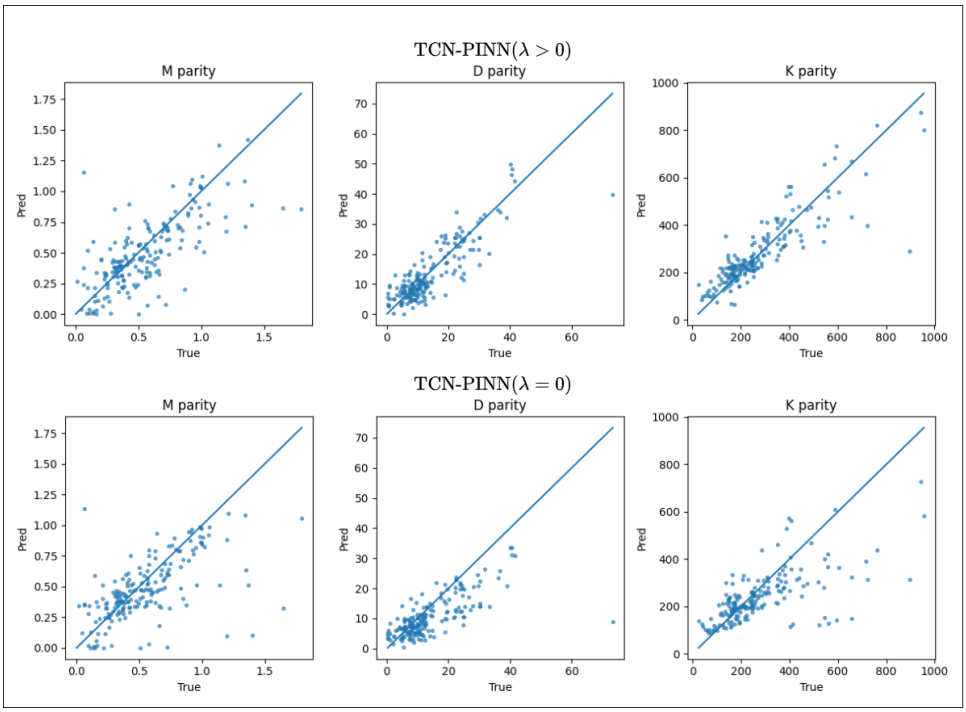

Fig. 23. Parity plots comparing predicted versus ground-truth impedance parameters for TCN-PINN models. Incorporating physics priors ($\lambda > 0$) yields tighter clustering along the identity line, particularly for damping and stiffness.

Appendix D

Joint Angle Capture for Multiple Participants

In this experiment, joint angles were estimated using three marker clusters attached to the forearm, upper arm, and shoulder. The relative orientations of these rigid bodies were used to approximate the arm's joint angles. While this approach provides a practical estimate of segment motion, its accuracy and generalizability across participants can be limited by non-anatomical marker placement.

A more robust and standardized approach is to follow the International Society of Biomechanics (ISB) recommendations, or equivalently, to use musculoskeletal modeling tools such as OpenSim, which implement similar anatomical conventions for defining joint coordinate systems. Using anatomical landmarks ensures consistent segment definitions across subjects and facilitates comparison with other biomechanical datasets.

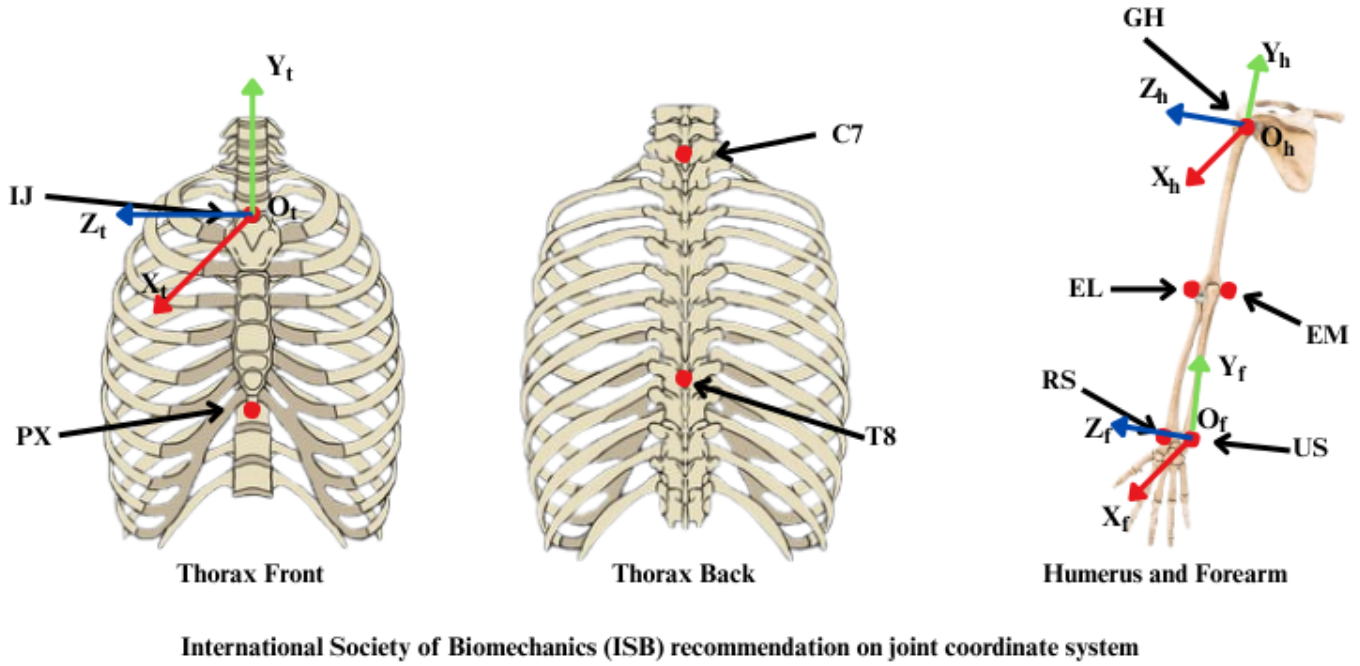

Fig. 24. ISB-recommended anatomical landmarks for defining thorax, humerus, and forearm coordinate systems.

Following ISB conventions, three primary rigid bodies are defined for estimating upper-limb joint motion:

1) **Thorax**: defines the global reference frame. Landmarks: IJ (suprasternal notch), PX (xiphoid process), C7, and T8.
2) **Humerus**: used to compute shoulder joint angles: flexion/extension, abduction/adduction, and internal/external rotation. Landmarks: AC (acromion), EL (lateral epicondyle), and EM (medial epicondyle).
3) **Forearm**: used to compute elbow flexion/extension and forearm pronation/supination. Landmarks: RS (radial styloid) and US (ulnar styloid).

The code used for estimating joint angles from the anatomical marker sites following these ISB definitions is available in the project repository referenced in *Appendix E*.

Appendix E

Code And Data Repository

The complete source code and methodology for setting up the experimental pipeline and neural network models are available at: `https://github.com/junglator/Physic-Informed-Arm-Impedance-Estimation-.git`.

Access can be requested for Code and Data.